MIT Open Access Articles

THE LUMINOSITY AND MASS FUNCTIONS OF LOW-MASS STARS IN THE GALACTIC DISK. II. THE FIELD

MIT Massachusetts Institute of Technology

DSpace@MIT

THE LUMINOSITY AND MASS FUNCTIONS OF LOW-MASS STARS IN THE GALACTIC DISK. II. THE FIELD

JOHN J. BOCHANSKI[1,2], SUZANNE L. HAWLEY[1], KEVIN R. COVEY[3], ANDREW A. WEST[2,4], I. NEILL REID[5],
DAVID A. GOLIMOWSKI[5], AND ŽELJKO IVEZIĆ[1]

[1] Astronomy Department, University of Washington, P.O. Box 351580, Seattle, WA 98195, USA; jjb@mit.edu
[2] Kavli Institute for Astrophysics and Space Research, Massachusetts Institute of Technology, Building 37, 77 Massachusetts Avenue, Cambridge, MA 02139, USA
[3] Department of Astronomy, Cornell University, 226 Space Sciences Building, Ithaca, NY 14853, USA
[4] Department of Astronomy, Boston University, 725 Commonwealth Avenue, Boston, MA 02215, USA
[5] Space Telescope Science Institute, 3700 San Martin Drive, Baltimore, MD 21218, USA
Received 2009 June 23; accepted 2010 April 21; published 2010 May 13

ABSTRACT

We report on new measurements of the luminosity function (LF) and mass function (MF) of field low-mass dwarfs derived from Sloan Digital Sky Survey Data Release 6 photometry. The analysis incorporates ∼15 million low-mass stars ($0.1\,\mathcal{M}_\odot < \mathcal{M} < 0.8\,\mathcal{M}_\odot$), spread over 8400 deg^2. Stellar distances are estimated using new photometric parallax relations, constructed from *ugriz* photometry of nearby low-mass stars with trigonometric parallaxes. We use a technique that simultaneously measures Galactic structure and the stellar LF from $7 < M_r < 16$. We compare the LF to previous studies and convert to an MF using the mass–luminosity relations of Delfosse et al. The system MF, measured over $-1.0 < \log \mathcal{M}/\mathcal{M}_\odot < -0.1$, is well described by a lognormal distribution with $\mathcal{M}_\circ = 0.25\,\mathcal{M}_\odot$. We stress that our results should not be extrapolated to other mass regimes. Our work generally agrees with prior low-mass stellar MFs and places strong constraints on future theoretical star formation studies.

Key words: brown dwarfs – Galaxy: stellar content – Galaxy: structure – stars: fundamental parameters – stars: late-type – stars: low-mass – stars: luminosity function, mass function

Online-only material: color figures

1. INTRODUCTION

Low-mass dwarfs ($0.1\,\mathcal{M}_\odot < \mathcal{M} < 0.8\,\mathcal{M}_\odot$) are, by number, the dominant stellar population of the Milky Way. These long-lived (Laughlin et al. 1997) and ubiquitous objects comprise ∼70% of all stars, yet their diminutive luminosities ($L \lesssim 0.05\,L_\odot$) have traditionally prohibited their study in large numbers. However, in recent years, the development of large-format CCDs has enabled accurate photometric surveys over wide solid angles on the sky, such as the Two Micron All Sky Survey (2MASS; Skrutskie et al. 2006) and the Sloan Digital Sky Survey (SDSS; York et al. 2000). These projects obtained precise ($\sigma \lesssim 5\%$) and deep ($r \sim 22$, $J \sim 16.5$) photometry of large solid angles ($\gtrsim 10^4$ deg^2). The resulting photometric data sets contain millions of low-mass stars, enabling statistical investigations of their properties. In particular, 2MASS photometry led to the discovery of two new spectral classes, *L* and *T* (Kirkpatrick et al. 1999; Burgasser et al. 2002), and was used to trace the structure of the Sagittarius dwarf galaxy (Majewski et al. 2003) with M giants. SDSS data led to the discovery the first field methane brown dwarf, which was the coolest substellar object known at the time of its discovery (Strauss et al. 1999). Other notable SDSS results include the discovery of new stellar streams in the halo (e.g., Yanny et al. 2003; Belokurov et al. 2006) and new Milky Way companions (e.g., Willman et al. 2005; Belokurov et al. 2007), as well as unprecedented in situ mapping of the stellar density (Jurić et al. 2008) and metallicity (Ivezić et al. 2008) distributions of the Milky Way and confirmation of the dual-halo structure of the Milky Way (Carollo et al. 2007). SDSS has proven to be a valuable resource for statistical investigations of the properties of low-mass stars, including their magnetic activity and chromospheric properties (West et al. 2004, 2008), flare characteristics

(Kowalski et al. 2009), and their use as tracers of Galactic structure (GS) and kinematics (Bochanski et al. 2007a; Fuchs et al. 2009).

Despite the advances made in other cool-star topics, two fundamental properties, the luminosity and mass functions, remain uncertain. The luminosity function (LF) describes the number density of stars as a function of absolute magnitude ($\Phi(M) = dN/dM$). The mass function (MF), typically inferred from the LF, is defined as the number density per unit mass ($\psi(\mathcal{M}) = dN/d\mathcal{M}$). For low-mass stars, with lifetimes much greater than the Hubble time, the observed present-day mass function (PDMF) in the field should trace the initial mass function (IMF). Following Salpeter (1955), the IMF has usually been characterized by a power law $\psi(\mathcal{M}) = dN/d\mathcal{M} \propto \mathcal{M}^{-\alpha}$, with the exponent α varying over a wide range, from 0.5 to 2.5. However, some studies have preferred a lognormal distribution. Previous investigations are summarized in Table 1 (MF) and Table 2 (LF), which show the total number of stars included and solid angle surveyed in each study.

Present uncertainties in the LF and MF can be attributed to disparate measurement techniques that are a result of trade-offs in observing strategy. Previous investigations of the LF and MF have fallen in one of two categories: nearby, volume-limited studies of trigonometric parallax stars; or pencil-beam surveys of distant stars over a small solid angle. Tables 1 and 2 detail the techniques used by modern investigations of the field LF and MF. In both cases, sample sizes were limited to a few thousand stars, prohibiting detailed statistical measurements. The solid angle shown in each table distinguishes the two types of surveys. There is considerable disagreement between the nearby, volume-limited investigations (Reid & Gizis 1997) and pencil-beam studies of distant stars (Martini & Osmer 1998; Zheng et al. 2001; Schultheis et al. 2006). It has been suggested

Table 1
Major Low-mass Field IMF Studies

Authors	N_{Stars}	Ω (sq. deg.)	Filter(s)	Depth	Mass Range	$\alpha, \mathcal{M}_\circ$	Notes
Salpeter (1955)	⋯	⋯	V	⋯	$0.3\,\mathcal{M}_\odot$–$10\,\mathcal{M}_\odot$	$\alpha = 2.35$	Compiled LFs from contemporaries[a]
Miller & Scalo (1979)	⋯	⋯	V	⋯	$0.1\,\mathcal{M}_\odot$–$60\,\mathcal{M}_\odot$	$\mathcal{M}_\circ \simeq 0.1\,\mathcal{M}_\odot$	Lognormal fit, Compilation of 3 field LFs[b]
Kroupa et al. (1990)	⋯	⋯	V	⋯	$0.1\,\mathcal{M}_\odot$–$0.9\,\mathcal{M}_\odot$	$\mathcal{M}_\circ \simeq 0.23\,\mathcal{M}_\odot$ $\alpha = 0.70$	Adopted LFs of Scalo (1986) and Stobie et al. (1989)
Kroupa et al. (1993)	⋯	⋯	V, I	⋯	$0.08\,\mathcal{M}_\odot$–$0.5\,\mathcal{M}_\odot$	$0.70 < \alpha < 1.85$	LF from Wielen et al. (1983) and Stobie et al. (1989)
Tinney (1993)	3,500	280	I, K	$I \lesssim 17.5$	$0.1\,\mathcal{M}_\odot$–$0.5\,\mathcal{M}_\odot$	⋯	Turnover at $0.25\,\mathcal{M}_\odot$
Reid & Gizis (1997)	151	$\delta > -30°$	V, I	$d < 8$ pc	$0.08\mathcal{M}_\odot$–$1.2\,\mathcal{M}_\odot$	$\alpha = 1.2$	Solar neighborhood[c]
Martini & Osmer (1998)	1,500	0.83	V, R	$V \lesssim 23.5$	$0.1\,\mathcal{M}_\odot$–$0.6\,\mathcal{M}_\odot$	1.3	
Zheng et al. (2001)	∼1,400	∼0.4	V, I	$18 \lesssim I \lesssim 24$	$0.1\,\mathcal{M}_\odot$–$0.6\,\mathcal{M}_\odot$	$\alpha = 0.45$	*HST* observations
Kroupa (2002)	⋯	⋯	V, I	⋯	$0.08\,\mathcal{M}_\odot$–$0.50\,\mathcal{M}_\odot$	$\alpha = 1.3$	Compiled contemporary LFs[d]
Reid et al. (2002)	558	3π ster.	B, V	$d \lesssim 20$ pc	$0.1\,\mathcal{M}_\odot$–$3.0\,\mathcal{M}_\odot$	$\alpha \simeq 1.3$	Solar Neighborhood Survey
Chabrier (2003a)	⋯	⋯	V, K	⋯	$0.1\,\mathcal{M}_\odot$–$1.0\,\mathcal{M}_\odot$	$\mathcal{M}_\circ = 0.22\,\mathcal{M}_\odot$	Review of contemporary field LFs[e]
Schultheis et al. (2006)	3,600	∼3	r', i'	$i' \sim 21$	$\mathcal{M} < 0.25\,\mathcal{M}_\odot$	$\alpha = 2.5$	CFHT MegaCAM observations
Covey et al. (2008)	∼29×10^3	30	i, J	$J = 16.2$	$0.1\,\mathcal{M}_\odot$–$0.8\,\mathcal{M}_\odot$	$\mathcal{M}_\circ = 0.29\,\mathcal{M}_\odot$	Matched SDSS and 2MASS observations
This study	∼15×10^6	8,400	r, i, z	$16 < r < 22$	$0.1\,\mathcal{M}_\odot$–$0.8\,\mathcal{M}_\odot$	$\mathcal{M}_\circ = 0.25\,\mathcal{M}_\odot$	SDSS observations

Notes.
[a] Salpeter averaged LFs from van Rhijn (1925, 1936) and Luyten (1939, 1941).
[b] Their adopted LF was averaged from the LFs of McCuskey (1966), Luyten (1968), and Wielen (1974).
[c] The "8 pc" sample was compiled by Reid & Gizis (1997), with later additions from Reid et al. (1999, 2003) and Cruz et al. (2007).
[d] Kroupa (2002) presents a comprehensive summary of MFs derived from the field and clusters over a wide mass range. For low-mass stars in the field, he refers to Reid et al. (1999), Herbst et al. (1999), Chabrier (2001), and Zheng et al. (2001).
[e] Chabrier (2003a) compared the LFs of Dahn et al. (1986), Henry & McCarthy (1990), and Zheng et al. (2001).

Table 2
Major Low-mass Stellar Field LF Studies

Authors	N_{Stars}	Ω (sq. deg.)	Filter(s)	Depth	Distance Method	Notes
Stobie et al. (1989)	178	18.88	V, I	$I < 16$	Phot. π	*VI* photometry
Henry et al. (1994)	92	$\delta > -25°$	V	$d = 5$ pc	Trig. π	Spec., CSN3 photometry
Reid et al. (1995)	520	$\delta > -30°$	V	$d \sim 20$ pc	Trig. π	Spec., CNS3 photometry[a]
Reid & Gizis (1997)	151	$\delta > -30°$	V	$d = 8$ pc	Trig. π	Spec., CNS3 photometry[b]
Martini & Osmer (1998)	4,005	0.83	V	$V \sim 23.5$	Phot. π	*UBVRI* photometry
Zheng et al. (2001)	1,413	∼0.4	V	$I \sim 26.5$	Phot. π	*HST* photometry [c]
Reid et al. (2002)	558	$\delta > -30°$	V	$d \sim 20$ pc	Trig. π	Spec., CNS3 photometry
Cruz et al. (2007)	99	14,823	J	$J \sim 17, d \sim 20$ pc	Phot. π, Trig. π	Spec., 2MASS photometry
Covey et al. (2008)	∼29×10^3	29	J	$J = 16.2$	Phot. π	SDSS and 2MASS photometry
This Study	∼15×10^6	8,417	r, J	$r = 22$	Phot. π	SDSS photometry

Notes.
[a] See Gliese & Jahreiss (1991) for details on sources of photometry.
[b] The 8 pc sample was further extended by Reid et al. (1999, 2003) and presented in J by Cruz et al. (2007).
[c] Some of the *Hubble Space Telescope* (*HST*) observations in this study were presented by Gould et al. (1996, 1997).

that this discrepancy is due to the presence of unresolved binary stars in the pencil-beam surveys (Kroupa et al. 1993; Chabrier 2003b), but this has not been shown conclusively (Reid & Gizis 1997). We investigate the effect of unresolved binaries in Section 5.5.

Using a sample drawn from SDSS, 2MASS and Guide Star Catalog photometry, and supplemented with SDSS spectroscopy, Covey et al. (2008) performed the largest field low-mass LF and MF investigations to date. Covering 30 deg² and containing ∼30,000 low-mass stars, their sample measured the LF using absolute magnitudes estimated from photometric colors and quantified the contamination rate by obtaining spectra of every red point source in a 1 deg² calibration region. The Covey et al. (2008) sample serves as a calibration study for the present work, as it quantified the completeness, bias, and contamination rate of the SDSS and 2MASS photometric samples. While their study focused on a limited sight line, the current investigation expands to the entire SDSS footprint, increasing the solid angle by a factor of ∼300.

In Section 2, we describe the SDSS photometry used to measure the field LF and MF. The color–absolute magnitude calibration is discussed in Section 3. In Section 4, we introduce a new technique for measuring the LF of large, deep photometric data sets and compare to previous analyses. The resulting "raw" LF is corrected for systematic effects such as unresolved binarity, metallicity gradients, and changes in GS in Section 5. The final LF and our MF are presented in Sections 6 and 7. Our conclusions follow in Section 8.

2. OBSERVATIONS

2.1. SDSS Photometry

The SDSS (York et al. 2000; Stoughton et al. 2002) employed a 2.5 m telescope (Gunn et al. 2006) at Apache Point Observatory (APO) to conduct a photometric survey in the optical *ugriz* filters (Fukugita et al. 1996; Ivezić et al. 2007). The sky was imaged using a time-delayed integration technique. Great circles on the sky were scanned along six camera columns, each

consisting of five 2048 × 2048 SITe/Tektronix CCDs with an exposure time of ∼54 s (Gunn et al. 1998). A custom photometric pipeline (Photo; Lupton et al. 2001) was constructed to analyze each image and perform photometry. Calibration onto a standard star network (Smith et al. 2002) was accomplished using observations from the "Photometric Telescope" (PT; Hogg et al. 2001; Tucker et al. 2006). Further discussion of PT calibrations for low-mass stars can be found in Davenport et al. (2007). Absolute astrometric accuracy is better than 0.″1 (Pier et al. 2003). Centered on the northern Galactic cap, the imaging data span ∼10,000 deg², and is 95% complete to $r \sim 22.2$ (Stoughton et al. 2002; Adelman-McCarthy et al. 2008). When the north Galactic pole was not visible from APO, ∼300 deg² were scanned along the $\delta = 0$ region known as "Stripe 82" to empirically quantify completeness and photometric precision (Ivezić et al. 2007). Over 357 million unique photometric objects have been identified in the latest public data release (DR7, Abazajian et al. 2009). The photometric precision of SDSS is unrivaled for a survey of this size, with typical errors $\lesssim$0.02 mag (Ivezić et al. 2004, 2007).

2.2. Sample Selection

We queried the SDSS catalog archive server (CAS) through the *casjobs* Web site (O'Mullane et al. 2005)[6] for point sources with the following criteria.

1. The observations fell within the Data Release 6-Legacy (DR6; Adelman-McCarthy et al. 2008) footprint. The equatorial and Galactic coordinate maps of the sample are shown in Figure 1.
2. The photometric objects were flagged as PRIMARY. This flag serves two purposes. First, it implies that the GOOD flag has been set, where GOOD ≡ !BRIGHT AND (!BLENDED OR NODEBLEND OR N_CHILD = 0). BRIGHT refers to duplicate detections of bright objects and the other set of flags ensures that stars were not deblended and counted twice. The PRIMARY flag indicates that objects imaged multiple times are only counted once 2.[7]
3. The object was classified morphologically as a star(TYPE = 6).
4. The photometric objects fell within the following brightness and color limits:

$$i < 22.0, z < 21.2$$
$$r - i \geqslant 0.3, i - z \geqslant 0.2.$$

The first two cuts extend past the 95% completeness limits of the survey ($i < 21.3$, $z < 20.5$; Stoughton et al. 2002), but more conservative completeness cuts are enforced below. The latter two cuts ensure that the stars have red colors typical of M dwarfs (Bochanski et al. 2007b; Covey et al. 2007; West et al. 2008).

This query produced 32,816,619 matches. To ensure complete photometry, we required $16 < r < 22$. These cuts conservatively account for the bright end of SDSS photometry, since the detectors saturate near the 15th magnitude (Stoughton et al. 2002). At the faint end, the $r < 22$ limit is slightly brighter than the formal 95% completeness limits. 23,323,453 stars remain after these brightness cuts.
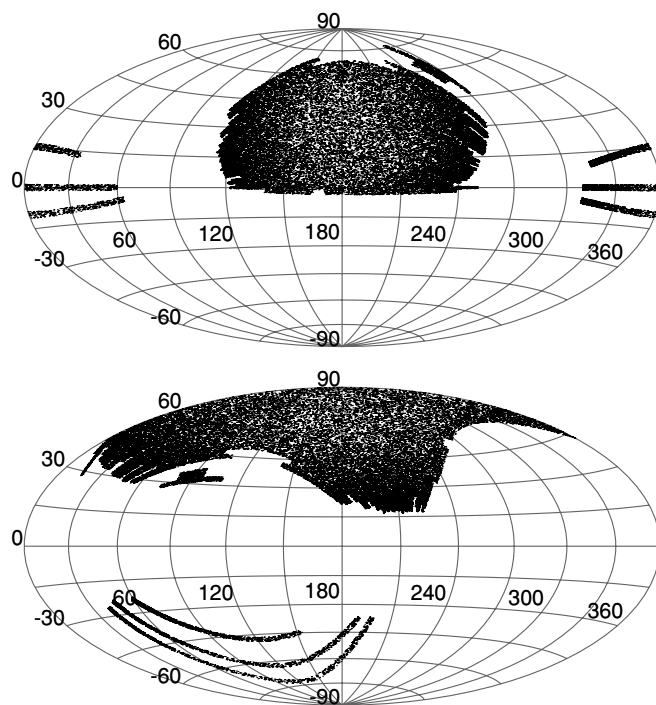
Figure 1. Aitoff projections of the SDSS DR6 Legacy footprint in equatorial (top panel) and Galactic (bottom panel) coordinates. To aid figure clarity, only 0.2% of the final sample is shown.

SDSS provides many photometric flags that assess the quality of each measurement. These flags are described in detail by Stoughton et al. (2002) and in the SDSS Web documentation.[8] With the following series of flag cuts, the ∼23 million photometric objects were cleaned to a complete, accurate sample. Since only the r, i, and z filters were used in this analysis, all of the following flags were only applied to those filters. The r-band distribution of sources is shown in Figure 2, along with the subset eliminated by each flag cut described below. The color–color diagrams for each of these subsets are shown in Figure 3.

Saturated photometry was removed by selecting against objects with the SATURATED flag set. As seen in Figure 2, this cut removes mostly objects with $r < 15$. However, there were some fainter stars within the footprint of bright, saturated stars. These stars are also marked as SATURATED and not included in our sample. NOTCHECKED was used to further clean saturated stars from the photometry. This flag marks areas on the sky where Photo did not search for local maxima, such as the cores of saturated stars. Similarly, we eliminated sources with the PEAKCENTER set, where the center of a photometric object is identified by the peak pixel and not a more sophisticated centroiding algorithm. As seen in Figure 2, both of these flags composed a small fraction of the total number of observations and are more common near the bright and faint ends of the photometry. Saturated objects and very low signal-to-noise observations will fail many of these tests.

The last set of flags examines the structure of the point-spread function (PSF) after it has been measured. The PSF_FLUX_INTERP flag is set when over 20% of the star's PSF is interpolated. While Stoughton et al. (2002) claim that this procedure generally provides trustworthy photometry, they
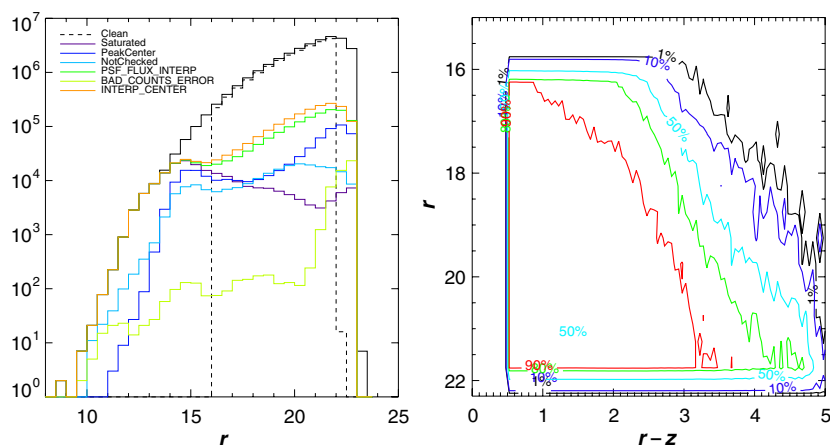
Figure 2. Left panel: histogram of *r*-band photometry (0.5 mag bins) showing the effects of flag cuts on the sample. Each flag is labeled with a different color as noted in the legend. The "clean" sample (dashed line) is complete from $16 < r < 22$. Each flag is plotted separately, but many objects with faulty photometry have multiple flags set. Right panel: percentage of stars retained after the described flag cuts as a function of color and brightness. Note that for the majority of the sample, over 90% of the stars are being retained. Each contour is labeled.

(A color version of this figure is available in the online journal.)
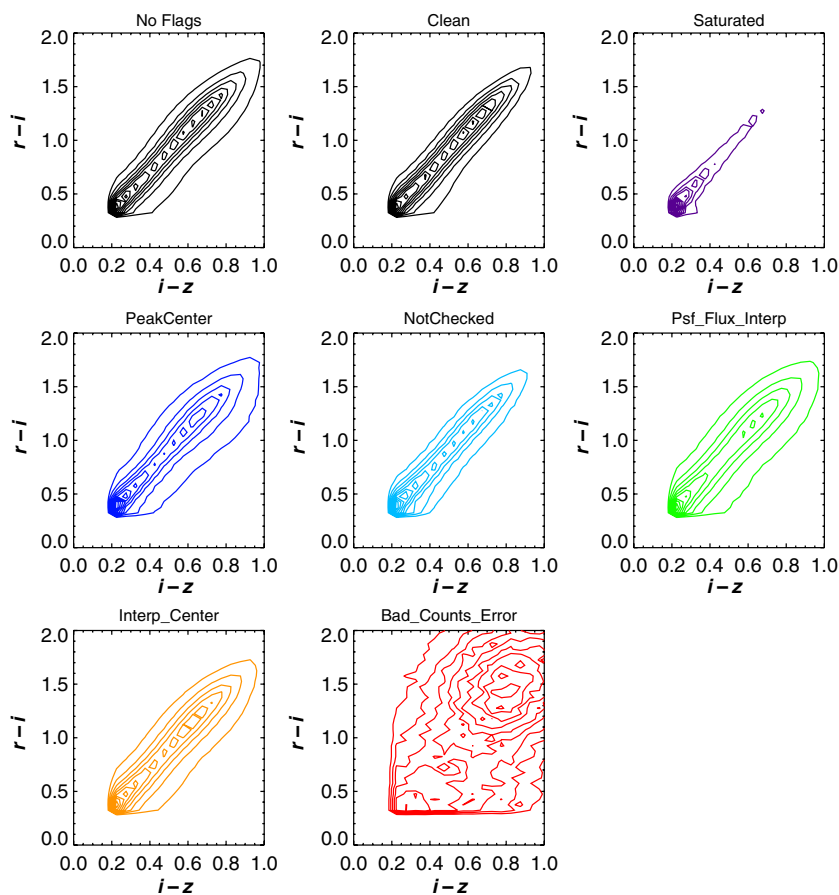
Figure 3. $r - i, i - z$ color–color diagrams for the various flag cuts discussed above. The contours increase at 10% intervals. Of note are the relatively wide loci of the objects with the PSF_FLUX_INTERP, PEAK_CENTER, and INTERP_CENTER flags set. BAD_COUNTS_ERROR objects demonstrate considerable scatter. SATURATED objects are mostly bluer, indicating that they are probably higher-luminosity stars.

(A color version of this figure is available in the online journal.)

warn of cases where this may not be true. Visual inspection of the $(r - i, i - z)$ color–color diagram in Figure 3 confirmed the latter, showing a wider locus than other flag cuts. The INTERP_CENTER flag is set when a pixel within three pixels of the center of a star is interpolated. The $(r - i, i - z)$ color–color diagram of objects with INTERP_CENTER set is also wide, and the fit to the PSF could be significantly af-

fected by an interpolated pixel near its center (Stoughton et al. 2002). Thus, stars with these flags set were removed. Finally, BAD_COUNTS_ERROR is set when a significant fraction of the star's PSF is interpolated over, and the photometric error estimates should not be trusted. Table 3 lists the number of stars in the sample with each flag set. For the final "clean" sample, we defined the following metaflag:
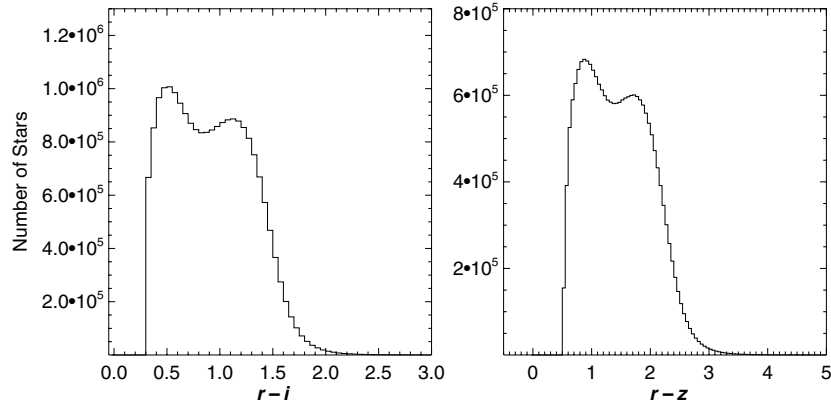
Figure 4. Histograms of color for the final stellar sample in $r - i$ and $r - z$.

Table 3
Flag Cuts in SDSS DR6 Sample

Flag	Number of Stars	Description
SATURATED	246,316	Pixel(s) saturated within the PSF
PSF_FLUX_INTERP	1,609,439	>20% of the PSF interpolated
INTERP_CENTER	1,993,063	Interpolated pixel within 3 pixels of the center
BAD_COUNTS_ERROR	97,697	Significant interpolation, underestimated errors
PEAKCENTER	598,108	Center found by peak pixel, centroiding failed
NOTCHECKED	230,375	Peak of PSF not examined, probably saturated
"CLEAN"	21,418,445 passed	Stars that passed quality and completeness cuts
"CUBE"	15,340,771 passed	"Clean" stars within a 4 kpc^3 cube

clean = (!SATURATED$_{r,i,z}$ AND !PEAKCENTER$_{r,i,z}$ AND !NOTCHECKED$_{r,i,z}$ AND !PSF_FLUX_INTERP$_{r,i,z}$ AND !INTERP_CENTER$_{r,i,z}$ AND !BAD_COUNTS_ERROR$_{r,i,z}$ AND ($16 < $ psfmag_r $ < 22$)).

After the flag cuts, the stellar sample was composed of 21,418,445 stars.

The final cut applied to the stellar sample was based on distance. As explained in Section 4.1, stellar densities were calculated within a $4 \times 4 \times 4$ kpc^3 cube centered on the Sun. Thus, only stars within this volume were retained, and the final number of stars in the sample is 15,340,771.[9]

In Figure 4, histograms of the $r - i$, $i - z$, and $r - z$ colors are shown. These color histograms map directly to absolute magnitude, since color–magnitude relations (CMRs) are used to estimate absolute magnitude and distance. The structure seen in the color histograms at $r-i \sim 1.5$ and $r-z \sim 2.2$ results from the convolution of the peak of the LF with the Galactic stellar density profile over the volume probed by SDSS. Removing the density gradients and normalizing by the volume sampled constitutes the majority of the effort needed to convert these color histograms into an LF. The $(g - r, r - i)$ and $(r - i, i - z)$ color–color diagrams are shown in Figure 5, along with the model predictions of Baraffe et al. (1998) and Girardi et al. (2004). It is clearly evident that the models fail to reproduce the stellar locus, with discrepancies as large as ∼1 mag. These models should not be employed as color–absolute magnitude relations for low-mass stars.

2.3. Star–Galaxy Separation

With any deep photometric survey, accurate star–galaxy separation is a requisite for many astronomical investigations. At faint magnitudes, galaxies far outnumber stars, especially at the

Galactic latitudes covered by SDSS. Star–galaxy identification is done automatically in the SDSS pipeline, based on the brightness and morphology of a given source. Lupton et al. (2001) investigated the fidelity of this process, using overlap between *HST* observations and early SDSS photometry. They showed that star–galaxy separation is accurate for more than >95% of objects to a magnitude limit of $r \sim 21.5$. Since the present sample extends to $r = 22$, we re-investigated the star–galaxy separation efficiency of the SDSS pipeline. We matched the SDSS pipeline photometry to the *HST* Advanced Camera for Surveys (ACS) images within the COSMOS (Scoville et al. 2007) footprint. The details of this analysis will be published in a later paper (J. J. Bochanski et al., 2010, in preparation). In Figure 6, we plot the colors and brightnesses of COSMOS galaxies identified as stars by the SDSS pipeline (red filled circles), along with a representative subsample of 0.02% of the stars in our sample. This figure demonstrates that for the majority of the stars in the present analysis, the SDSS morphological identifications are adequate, and contamination by galaxies is not a major systematic.

3. CALIBRATION: PHOTOMETRIC PARALLAX

Accurate absolute magnitude estimates are necessary to measure the stellar field LF. Trigonometric parallaxes, such as those measured by *Hipparcos* (ESA 1997; van Leeuwen 2007), offer the most direct method for calculating absolute magnitude. Unfortunately, trigonometric parallaxes are not available for many faint stars, including the overwhelming majority of the low-mass dwarfs observed by SDSS. Thus, other methods must be employed to estimate a star's absolute magnitude (and distance). Two common techniques, known as photometric parallax and spectroscopic parallax, use a star's color or spectral type, respectively. These methods are calibrated by sources with known absolute magnitudes (nearby trigonometric parallax

---

9 The reported number is based on the $(M_r, r - z)$ CMR. As explained in Section 5, changes to the CMR can add or subtract stars from the volume.
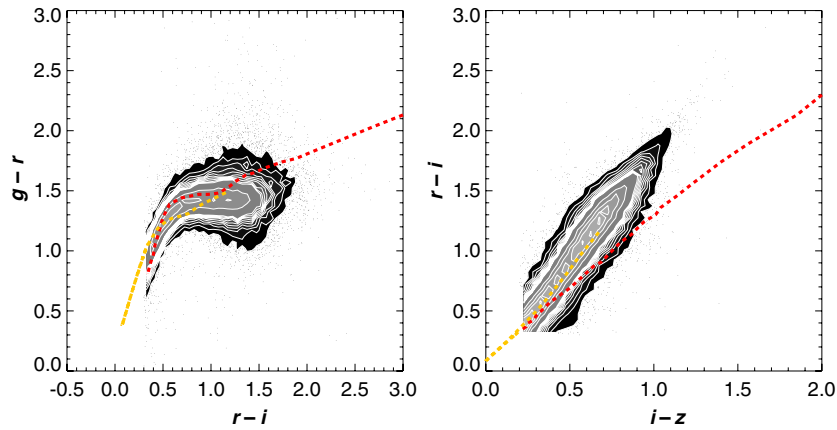
Figure 5. Color–color diagrams of the final photometric sample with the 5 Gyr isochrones of Baraffe et al. (1998, red dashed line) and Girardi et al. (2004, yellow dashed line) overplotted. The contours represent 0.2% of our entire sample, with contours increasing every 10 stars per 0.05 color–color bin. Note that the model predictions fail by nearly 1 mag in some locations of the stellar locus.
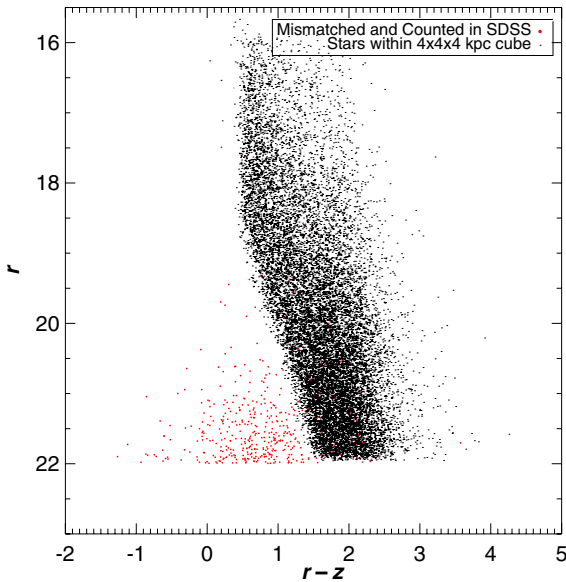
(A color version of this figure is available in the online journal.)

Figure 6. Hess diagram for objects identified as stars in the SDSS pipeline, but as galaxies with high-resolution ACS imaging in the COSMOS footprint (red filled circles). The black points show 0.02% of the final stellar sample used in the present analysis. Note that galaxy contamination is the most significant at faint, blue colors. These colors and magnitudes are not probed by our analysis, since these objects lie beyond our $4 \times 4 \times 4$ kpc distance cut.

(A color version of this figure is available in the online journal.)

stars, clusters, etc.), and mathematical relations are fitted to their color (or spectral type)—absolute magnitude locus. Thus, the color of a star can be used to estimate its absolute magnitude, and in turn, its distance, by the well-known distance modulus $(m - M)$:

$$m_{\lambda,1} - M_{\lambda,1}(m_{\lambda,1} - m_{\lambda,2}) = 5\log d - 5, \qquad (1)$$

where d is the distance, $m_{\lambda,1}$ is the apparent magnitude in one filter, and $m_{\lambda,1} - m_{\lambda,2}$ is the color from two filters, which is used to calculate the absolute magnitude, $M_{\lambda,1}$.

There have been multiple photometric parallax relations,[10] as shown in Figure 7, constructed for low-mass stars observed by SDSS (Hawley et al. 2002; Williams et al. 2002; West et al.

---
[10] Photometric parallax relations are often referred to as color–magnitude relations. We use both names interchangeably throughout this manuscript.
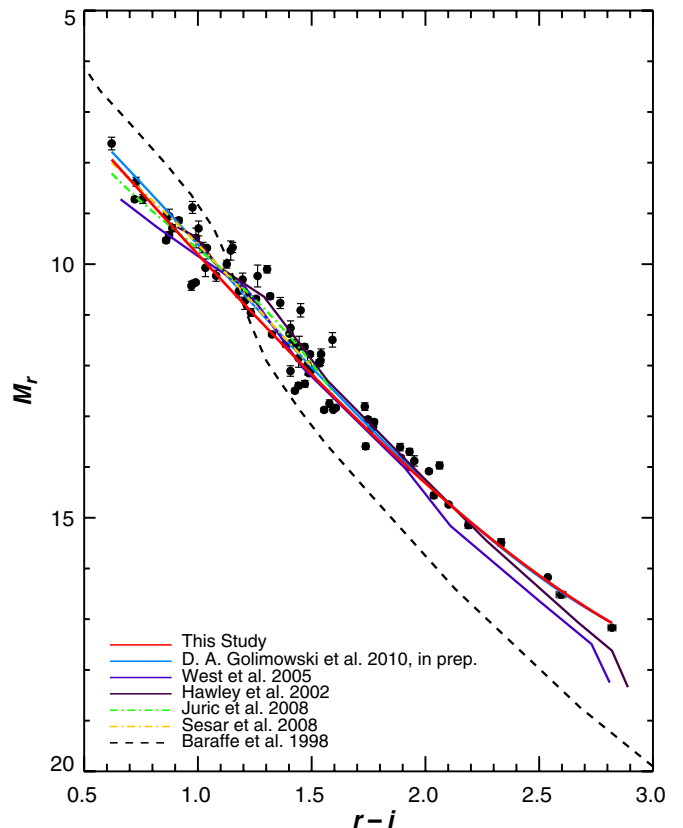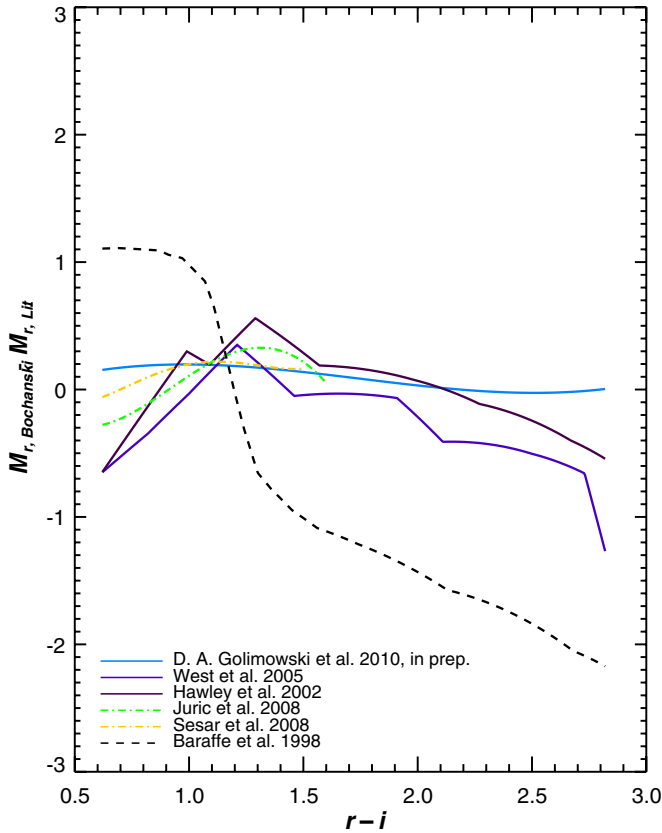

Figure 7. M_r vs. $r - i$ CMD. The parallax stars from the nearby star sample are shown as filled circles, and the best-fit line from Table 4 is the solid red line. Other existing parallax relations are plotted for comparison: West et al. (2005, purple dash-dotted line), Jurić et al. (2008, green dash-dotted line), Sesar et al. (2008, yellow dash-dotted line), and D. A. Golimowski et al. (2010, in preparation, solid blue line). The original West et al. (2005) relations have been transformed using the data from their Table 1. In addition, the 5 Gyr isochrone from the Baraffe et al. (1998) models appears as the dashed line.

(A color version of this figure is available in the online journal.)

2005; Jurić et al. 2008; Sesar et al. 2008; D. A. Golimowski et al. 2010, in preparation). There is a spread among the relations, seen in Figure 8, which are valid over different color ranges. Additional photometry in $ugrizJHK_s$ of a large sample of nearby

Figure 8. Differences between the M_r vs. $r - i$ relations in Figure 7. The line styles are the same as Figure 7. Note that the observed photometric parallax relations generally agree to ~0.5 mag, while the 5 Gyr isochrone of Baraffe et al. (1998) does not agree with the empirical results.

(A color version of this figure is available in the online journal.)

stars with well-measured trigonometric parallaxes is required to provide a reliable relation. Fortunately, an observing program led by D. A. Golimowski et al. (2010, in preparation) acquired such observations and they kindly provided their data prior to publication. The resulting CMRs are used to estimate the absolute magnitude and distance to all the stars in our sample, as described below.

3.1. Photometric Telescope Photometry

The nearby star survey (D. A. Golimowski et al. 2010, in preparation) targeted stars with the colors of low-mass dwarfs and precise trigonometric parallaxes. The majority of targets were drawn from the Research Consortium on Nearby Stars (RECONS) catalog (e.g., Henry et al. 1994, 2004; Kirkpatrick et al. 1995). Most of the stars selected from the RECONS sample are within 10 pc, with good parallactic precision ($\sigma_\pi/\pi \lesssim 0.1$). In addition to RECONS targets, the nearby sample included K dwarfs from the Luyten (1979) and Giclas et al. (1971) proper motion surveys. Parallax measurements for these additional stars were obtained from the *Hipparcos* (ESA 1997) or General Catalogue of Trigonometric Stellar Parallaxes (the "Yale" catalog; van Altena et al. 1995) surveys.

Near-infrared JHK_s photometry was obtained from the 2MASS Point Source Catalog (Cutri et al. 2003). Acquiring $ugriz$ photometry proved more problematic. Since typical SDSS photometry saturates near $r \sim 15$, most of the nearby stars were too bright to be directly imaged with the 2.5 m telescope. In-

stead, the 0.5 m PT was used to obtain $(ugriz)'$ photometry[11] of these stars. The PT was active every night; the 2.5 m telescope was used in imaging mode during the SDSS, observing patches of the nightly footprint to determine the photometric solution for the night, and to calibrate the zero point of the 2.5 m observations (Smith et al. 2002; Tucker et al. 2006). D. A. Golimowski et al. (2010, in preparation) obtained $(ugriz)'$ photometry of the parallax sample over 20 nights for 268 low-mass stars. The transformations of Tucker et al. (2006) and the Davenport et al. (2007) corrections were applied to the nearby star photometry to transform the "primed" PT photometry to the native "unprimed" 2.5 m system (see Davenport et al. 2007 for more details).

To produce a reliable photometric parallax relation, the following criteria were imposed on the sample. First, stars with large photometric errors ($\sigma > 0.1$ mag) in the $griz$ bands were removed. Next, high signal-to-noise 2MASS photometry was selected, by choosing stars with their ph_qual flag equal to "AAA." This flag corresponds to a signal-to-noise ratio >10 and photometric uncertainties <0.1 mag in the JHK_s bands. Next, a limit on parallactic accuracy of $\sigma_\pi/\pi < 0.10$ was enforced. It ensured that the bias introduced by a parallax-limited sample, described by Lutz & Kelker (1973), is minimized. Since many of the stars in the nearby star sample have precise parallaxes ($\sigma_\pi/\pi < 0.04$), the Lutz–Kelker correction is essentially negligible (< -0.05; Hanson 1979). Finally, contaminants such as known subdwarfs, known binaries, suspected flares, or white dwarfs were culled from the nearby star sample.

3.2. Additional Photometry

To augment the original PT observations, we searched the literature for other low-mass stars with accurate parallaxes and $ugriz$ and JHK_s photometry. The studies of Dahn et al. (2002) and Vrba et al. (2004) supplemented the original sample and provided accurate parallaxes ($\sigma_\pi/\pi \lesssim 0.1$) of late M and L dwarfs. Several of those stars were observed with the SDSS 2.5 m telescope, obviating the need for transformations between the primed and unprimed $ugriz$ systems. Six late M and L dwarfs were added from these catalogs, extending the parallax sample in color from $r - i \sim 2.5$ to $r - i \sim 3.0$ and in M_r from 16 to 20. Our final sample is given in Bochanski (2008).

3.3. Color–Magnitude Relations

Multiple color–absolute magnitude diagrams (CMDs) in the $ugriz$ and JHK_s bandpasses were constructed using the photometry and parallaxes described above. The CMDs were individually inspected, fitting the main sequence with linear, second-, third-, and fourth-order polynomials. Piecewise functions were also tested, placing discontinuities by eye along the main sequence. There is an extensive discussion in the literature of a "break" in the main sequence near spectral type M4 (or $V - I \sim 2.8$; see Hawley et al. 1996; Reid & Gizis 1997; Reid & Cruz 2002; Reid & Hawley 2005). Certain colors, such as $V - I$, show evidence of a break (Figure 10 of Reid & Cruz 2002), while other colors, such as $V - K$, do not (Figure 9 of Reid & Cruz 2002). We did not enforce a break in our fits. Finally, the rms scatter about the fit for each CMD was computed, and the relation that produced the smallest scatter for each color–absolute magnitude combination was retained. Note that the rms scatter was dominated by the intrinsic width of the

---

[11] $(ugriz)'$ refers to $u'g'r'i'z'$ photometry, which is defined by the standard stars of Smith et al. (2002) observed by the USNO 1 m telescope.

Table 4
Color–Absolute Magnitude Relations in the *ugriz* System

Abs. Mag.	Color Range	Best Fit	σ_{M_r}
M_r	$0.50 < r - z < 4.53$	$5.190 + 2.474\,(r-z) + 0.4340\,(r-z)^2 - 0.08635\,(r-z)^3$	0.394
M_r	$0.62 < r - i < 2.82$	$5.025 - 4.548\,(r-i) + 0.4175\,(r-i)^2 - 0.18315\,(r-i)^3$	0.403
M_r	$0.32 < i - z < 1.85$	$4.748 + 8.275\,(i-z) + 2.2789\,(i-z)^2 - 1.5337\,(i-z)^3$	0.481
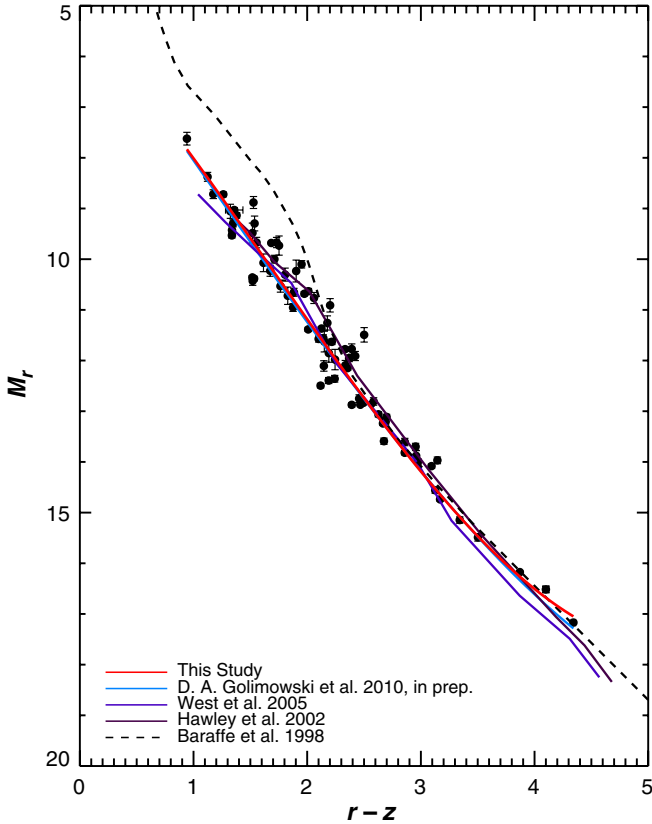
Figure 9. M_r vs. $r - z$ CMD. Symbols and lines are the same as Figure 7.
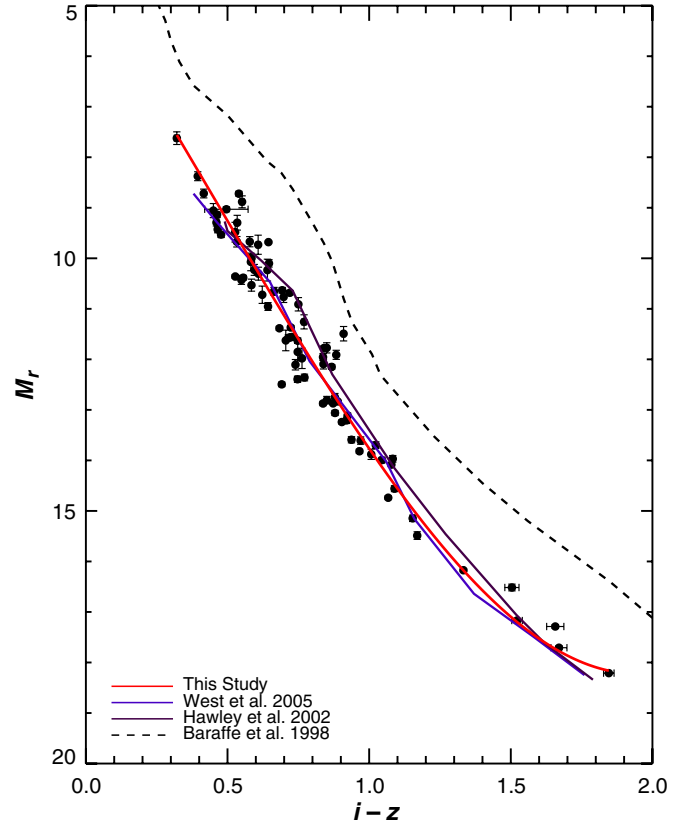(A color version of this figure is available in the online journal.)

Figure 10. M_r vs. $i - z$ CMD. Same symbol definitions as Figures 7 and 9. Note the very poor agreement between the observations and model predictions.
(A color version of this figure is available in the online journal.)

main sequence, as both our photometry and distances have small (∼2%) uncertainties.

We present three different CMRs: $(M_r, r - i)$, $(M_r, r - z)$, and $(M_r, i - z)$ in Table 4. M_r was used for absolute magnitude, as it contains significant flux in all late-type stars. The $r - z$ color has the longest wavelength baseline and small residual rms scatter ($\sigma \lesssim 0.40$ mag). Other long baseline colors ($g - r$, $g - z$) are metallicity sensitive (West et al. 2004; Lépine & Scholz 2008), but most of our sample does not have reliable g-band photometry. The adopted photometric parallax relations in these colors did not include any discontinuities, although we note a slight increase in the dispersion of the main sequence around $M_r \sim 12$. The final fits are shown in Figures 7, 9, and 10, along with other published photometric parallax relations in the *ugriz* system.

4. ANALYSIS

Our photometric sample comprises a data set 3 orders of magnitude larger (in number) than any previous LF study (see Table 2). Furthermore, it is spread over 8400 deg^2, nearly 300 times larger than the sample analyzed by Covey et al. (2008). This large sky coverage represents the main challenge in measuring the LF from this sample. Most of the previous studies in Table 2 either assumed a uniform density distribution (for nearby stars) or calculated a Galactic density profile, $\rho(r)$, along one line of sight. With millions of stars spread over nearly 1/4 of the sky, numerically integrating Galactic density profiles for each star is computationally prohibitive.

To address this issue, we introduced the following technique for measuring the LF. First, absolute magnitudes were assigned, and distances to each star were computed using the $r - z$ and $r - i$ CMRs from Table 4. Each CMR was processed separately. Next, a small range in absolute magnitude (0.5 mag) was selected, and the stellar density was measured in situ as a function of Galactic radius (R) and Galactic height (Z). This range in absolute magnitude was selected to provide high resolution in the LF, while maintaining a large number of stars ($\sim 10^6$) in each bin. Finally, a Galactic profile was fitted to the R, Z density maps, solving for the shape of the thin and thick disks, as well as the local density. The LF was then constructed by combining the local density of each absolute magnitude slice.

4.1. Stellar Density Maps

To assemble an (R, Z) density map, an accurate count of the number of stars in a given R, Z bin, as well as the volume
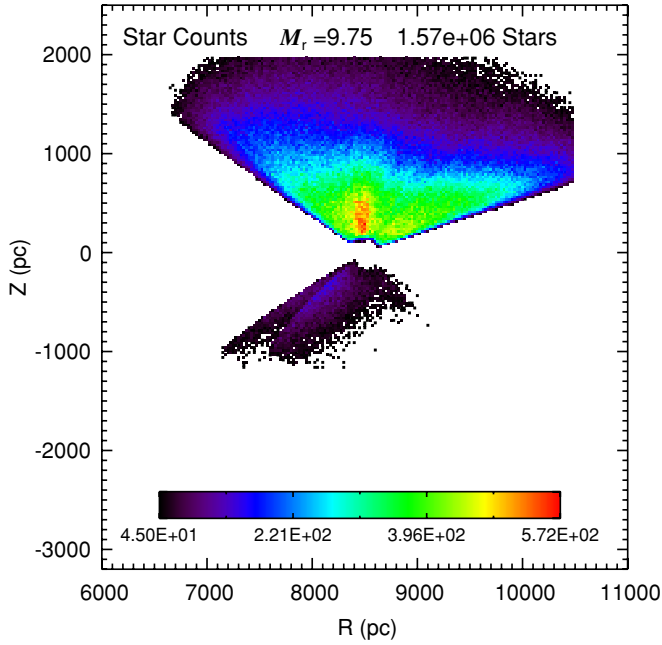
Figure 11. Star counts as a function of Galactic R and Z for a 0.5 mag slice in absolute magnitude centered on $M_r = 9.75$. The color bar on the lower part of the plot displays the scale of the image, with redder colors corresponding to larger stellar counts. The number of stars in this absolute magnitude slice is at the top of the plot. The majority of the stars in the sample were found in the northern Galactic hemisphere, since SDSS was centered on the northern Galactic cap.

(A color version of this figure is available in the online journal.)

spanned by each bin, was required. A cylindrical (R, Z, ϕ) coordinate system was taken as the natural coordinates of stellar density in the Milky Way. In this frame, the Sun's position was set at $R_\odot = 8.5$ kpc (Kerr & Lynden-Bell 1986) and $Z_\odot = 15$ pc above the plane (Cohen 1995; Ng et al. 1997; Binney et al. 1997). Azimuthal symmetry was assumed (and was recently verified by Jurić et al. 2008 and found to be appropriate for the local Galaxy). The following analysis was carried out in R and Z. We stress that we are not presenting any information on the $\phi = 0$ plane. Rather, the density maps are summed over ϕ, collapsing the three-dimensional SDSS volume into a two-dimensional density map.

The coordinate transformation from a spherical coordinate system (ℓ, b, and d) to a cylindrical (R, Z) system was performed with the following equations:

$$R = \sqrt{(d \cos b)^2 + R_\odot(R_\odot - 2d \cos b \cos \ell)} \qquad (2)$$

$$Z = Z_\odot + d \sin(b - \arctan(Z_\odot/R_\odot)), \qquad (3)$$

where d was the distance (as determined by Equation (1) and the (M_r, $r - z$) CMR), ℓ and b are the Galactic longitude and latitude, respectively, and $R_\odot$ and $Z_\odot$ are the positions of the Sun, as explained above.[12] The density maps were binned in R and Z. The bin width needed to be large enough to contain many stars (to minimize Poisson noise) but small enough to accurately resolve the structure of the thin and thick disks. The R, Z bin size was set at 25 pc. An example of the star counts as a function of R and Z is shown in Figure 11.

---

[12] Note that Equation (3) should contain a term with ℓ. We ignore this term due to its small size relative to the $d \sin b$ term.
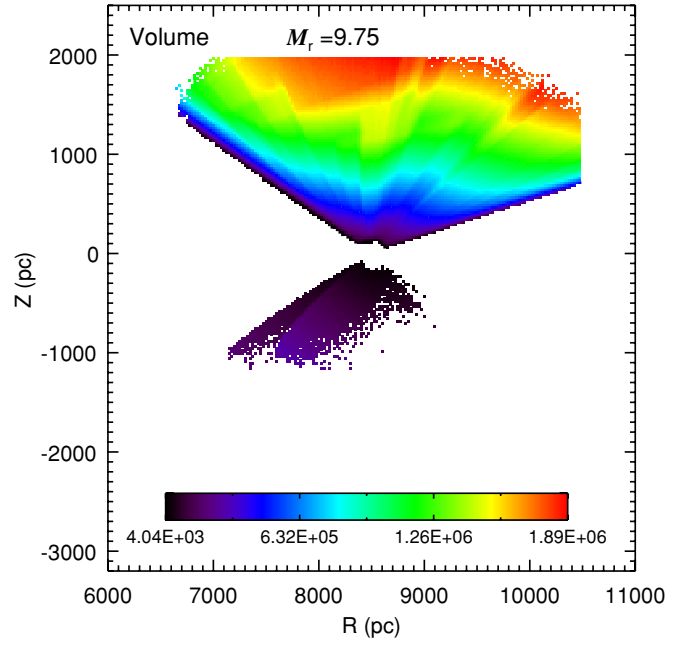

Figure 12. Volume probed by SDSS imaging as a function of Galactic R and Z for one 0.5 mag slice at $M_r = 9.75$. The corresponding scale (in pc^3) is at the bottom of the plot, with redder colors corresponding to larger volumes.

(A color version of this figure is available in the online journal.)

The volume sampled by each R, Z bin was estimated with the following numerical method. A $4 \times 4 \times 4$ kpc^3 cube of "test" points was laid down, centered on the Sun, at uniform intervals 1/10th the R, Z bin size (every 2.5 pc). This grid discretizes the volume, with each point corresponding to a fraction of the total volume. Here, the volume associated with each grid point was $k = 2.5^3$ pc^3 point^{-1} or 15.625 pc^3 point^{-1}. The volume of an arbitrary shape is straightforward to calculate: simply count the points that fall within the shape and multiply by k. The α, δ, and distance of each point were calculated and compared to the SDSS volume. The number of test points in each R, Z bin was summed and multiplied by k to obtain the final volume corresponding to that R, Z bin. This process was repeated for each absolute magnitude slice. The maximum and minimum distances were calculated for each absolute magnitude slice (corresponding to the faint and bright apparent magnitude limits of the sample), and only test points within those bounds were counted. The same volume was used for all stars within the sample. The bluer stars in our sample were found at distances beyond 4 kpc, but computing volumes at these distances would be computationally prohibitive. Furthermore, this method minimizes galaxy contamination, which is largest for bluer, faint objects (see Section 2.3). Since the volumes are fully discretized, the error associated with N_{points} is Poisson-distributed. A fiducial example of the volume calculations is shown in Figure 12.

After calculating the volume of each R, Z bin, the density (in units of stars pc^{-3}) is simply,

$$\rho(R, Z) = \frac{N(R, Z)}{V(R, Z)}, \qquad (4)$$

with the error given by,

$$\sigma_\rho = \rho \sqrt{\left(\frac{\sqrt{N(R, Z)}}{N(R, Z)}\right)^2 + \left(\frac{k\sqrt{N_{\mathrm{points}}(R, Z)}}{V(R, Z)}\right)^2}, \qquad (5)$$
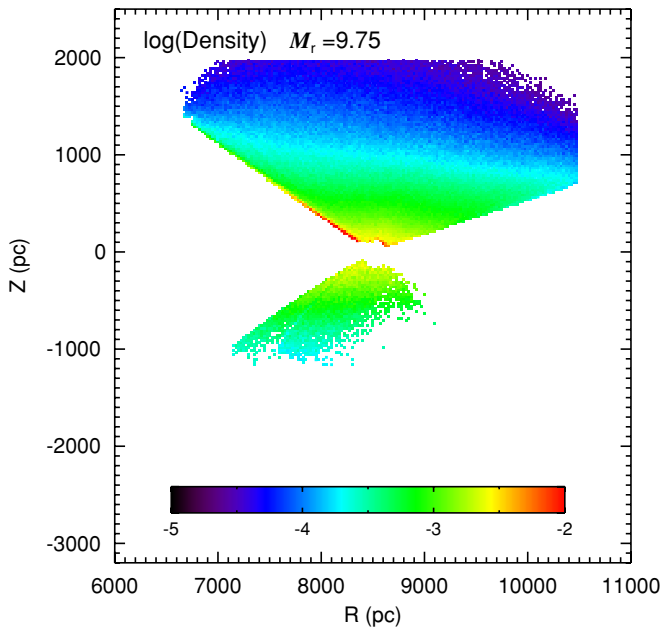
Figure 13. Density (in stars pc^{-3}) as a function of Galactic R and Z. The logarithmic scale is shown beneath the density map, with redder colors corresponding to larger densities. The disk structure of the Milky Way is clearly evident, with a smooth decline toward larger R, and an increase in density approaching the plane ($Z = 0$).

(A color version of this figure is available in the online journal.)

where $N(R, Z)$ is the star counts in each R, Z bin and $V(R, Z)$ is the corresponding volume. Fiducial density and error maps are shown in Figures 13 and 14. Note that the error in Equation (5) is dominated by the first term on the right-hand side. While a smaller k could make the second term less significant, it would be computationally prohibitive to include more test points. We discuss systematic errors which may influence the measured density in Section 5.

4.2. Galactic Model Fits

Using the method described above, (R, Z) stellar density maps were constructed for each 0.5 mag slice in M_r, from $M_r = 7.25$ to $M_r = 15.75$, roughly corresponding to spectral types M0–M8. The bin size in each map was constant, at 25 pc in the R and Z directions. For R, Z bins with density errors (Equation (5)) of $<15\%$, the following disk density structure was fitted:

$$\rho_{\text{thin}}(R, Z) = \rho_\circ f e^{\left(-\frac{R-R_\odot}{R_{\circ,\text{thin}}}\right)} e^{\left(-\frac{|Z|-Z_\odot}{Z_{\circ,\text{thin}}}\right)} \qquad (6)$$

$$\rho_{\text{thick}}(R, Z) = \rho_\circ (1 - f) e^{\left(-\frac{R-R_\odot}{R_{\circ,\text{thick}}}\right)} e^{\left(-\frac{|Z|-Z_\odot}{Z_{\circ,\text{thick}}}\right)} \qquad (7)$$

$$\rho(R, Z) = \rho_{\text{thin}}(R, Z) + \rho_{\text{thick}}(R, Z), \qquad (8)$$

where $\rho_\circ$ is the local density at the solar position ($R_\odot = 8500$ pc, $Z_\odot = 15$ pc), f is the fraction of the local density contributed by the thin disk, $R_{\circ,\text{thin}}$ and $R_{\circ,\text{thick}}$ are the thin and thick disk scale lengths, and $Z_{\circ,\text{thin}}$ and $Z_{\circ,\text{thick}}$ are the thin and thick disk scale heights, respectively. Since the density maps are dominated by nearby disk structure, the halo was neglected. Furthermore, Jurić et al. (2008) demonstrated that the halo structure is only important at $|Z| > 3$ kpc, well outside the volumes probed here. Restricting the sample to bins with density errors $<15\%$ ensures that they are well populated by stars, have
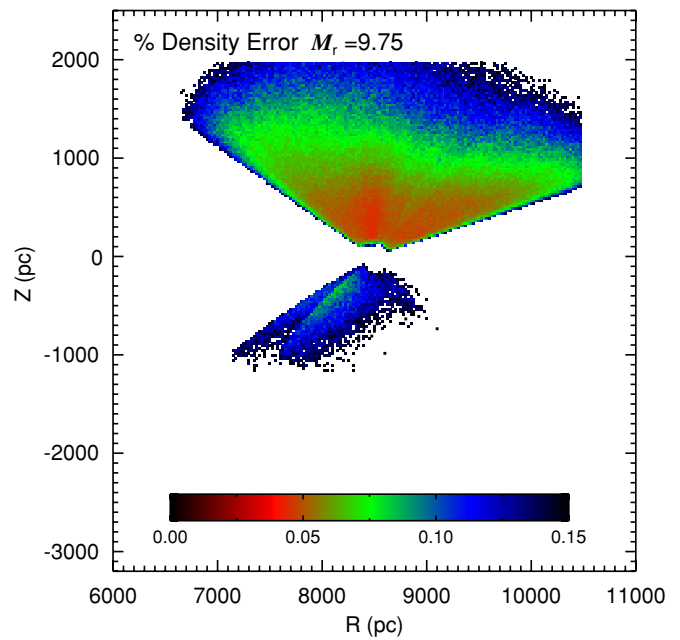

Figure 14. Fractional error in density as a function of R and Z. As in the previous figures, the scale is below the map, with bluer colors indicating larger errors. The errors, calculated in Equation (5), are $\lesssim 7\%$ for the majority of the sample.

(A color version of this figure is available in the online journal.)

precise volume measurements, and should accurately trace the underlying Milky Way stellar distribution. Approximately 50% of the R, Z bins have errors $\gtrsim 15\%$, while containing $>90\%$ of the stars in the sample.

The density maps were fitted using Equation (8) and a standard Levenberg–Marquardt algorithm (Press et al. 1992), using the following approach. First, the thin and thick disk scale heights and lengths, and their relative scaling, were measured using 10 absolute magnitude slices, from $M_r = 7.25$ to 11.75. These relatively more luminous stars yield the best estimates for GS parameters. Including lower-luminosity stars biases the fits, artificially shrinking the scale heights and lengths to compensate for density differences between a small number of adjacent R, Z bins. The scale lengths and heights and their relative normalization were fitted for the entire $M_r = 7.25$–11.75 range simultaneously. The resulting GS parameters ($Z_{\text{o,thin}}, Z_{\text{o,thick}}, R_{\text{o,thin}}, Z_{\text{o,thick}}, f$) are listed in Table 5 as raw values, not yet corrected for systematic effects (see Section 5 and Table 6). After the relative thin/thick normalization (f) and the scale heights and lengths of each component are fixed, the local densities were fitted for each absolute magnitude slice, using a progressive sigma clipping method similar to that of Jurić et al. (2008). This clipping technique excludes obvious density anomalies from biasing the final best fit. First, a density model was computed, and the standard deviation (σ) of the residuals was calculated. The R, Z density maps were refitted and bins with density residuals greater than 50σ are excluded. This process was repeated multiple times, with σ smoothly decreasing by the following series: $\sigma = (40, 30, 20, 10, 5)$. An example LF, constructed from the local densities of each absolute magnitude slice and derived from the M_R, $r - z$ CMR, is shown in Figure 15.

5. SYSTEMATIC CORRECTIONS

The observed LF is subject to systematics imposed by nature, such as unresolved binarity and metallicity gradients, as well as

Table 5
Measured Galactic Structure

Property	Raw Value	Uncertainty
$Z_{\rm o,thin}$	255 pc	12 pc
$R_{\rm o,thin}$	2200 pc	65 pc
$Z_{\rm o,thick}$	1360 pc	300 pc
$R_{\rm o,thick}$	4100 pc	740 pc
f	0.97	0.006

Table 6
Bias-corrected Galactic Structure

Property	Corrected Value	Uncertainty
$Z_{\rm o,thin}$	300 pc	15 pc
$R_{\rm o,thin}$	3100 pc	100 pc
$Z_{\rm o,thick}$	2100 pc	700 pc
$R_{\rm o,thick}$	3700 pc	800 pc
f	0.96	0.02

Figure 15. Raw r-band LF for the stellar sample, using the $(M_r, r - z)$ CMR. Note the smooth behavior, with a peak near $M_r \sim 11$, corresponding to a spectral type of $\sim$M4. The error bars (many of which are smaller than the points) are the formal uncertainties from fitting the local densities in each 0.5 mag absolute magnitude slice in stellar density.

those from the observations and analysis, e.g., Malmquist bias. The systematic differences manifested in different CMRs, which vary according to stellar metallicity, interstellar extinction, and color, are isolated and discussed in Sections 5.1 and 5.2, and the results are used in Section 5.3 to estimate the systematic uncertainties in the LF and GS.

Malmquist bias (Section 5.4) and unresolved binarity (Section 5.5) were quantified using Monte Carlo (MC) models. Each model was populated with synthetic stars that were consistent with the observed GS and LF. The mock stellar catalog was analyzed with the same pipeline as the actual observations and the differences between the input and "observed" GS and LF were used to correct the observed values.

5.1. Systematic CMRs: Metallicity

A star with low metallicity will have a higher luminosity and temperature compared to its solar-metallicity counterpart of the same mass, as first described by Sandage & Eggen (1959). However, at a fixed color, stars with lower metallicities have fainter absolute magnitudes. Failing to account for this effect artificially brightens low-metallicity stars, increasing their estimated distance. This inflates densities at large distances, increasing the observed scale heights (e.g., King et al. 1990).

Quantifying the effects of metallicity on low-mass dwarfs is complicated by multiple factors. First, direct metallicity measurements of these cool stars are difficult (e.g., Woolf & Wallerstein 2006; Johnson & Apps 2009), as current models do not accurately reproduce their complex spectral features. Currently, measurements of metallicity-sensitive molecular band heads (CaH and TiO) are used to estimate the metallicity of M dwarfs at the $\sim$1 dex level (see Gizis 1997; Lépine et al. 2003; Burgasser & Kirkpatrick 2006; West et al. 2008), but detailed measurements are only available for a few stars. The effects of metallicity on the absolute magnitudes of low-mass stars are poorly constrained. Accurate parallaxes for nearby subdwarfs do exist (Monet et al. 1992; Reid 1997; Burgasser et al. 2008), but measurements of their precise metal abundances are difficult given the extreme complexity of calculating the opacity of the molecular absorption bands that dominate the spectra of M dwarfs. Observations of clusters with known metallicities could mitigate this problem (Clem et al. 2008; An et al. 2008), but there are no comprehensive observations in the *ugriz* system that probe the lower main sequence.
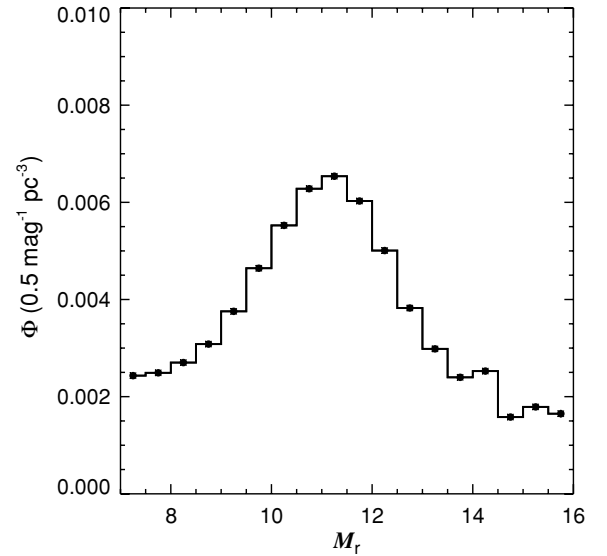
To test the systematic effects of metallicity on this study, the ([Fe/H],ΔM_r) relation from Ivezić et al. (2008) was adopted. We note that this relation is appropriate for more luminous F and G stars, near the main-sequence turnoff, but should give us a rough estimate for the magnitude offset. The adopted Galactic metallicity gradient is

$$[{\rm Fe/H}] = -0.0958 - 2.77 \times 10^{-4}|Z|. \qquad (9)$$

At small Galactic heights ($Z \lesssim 100$ pc), this linear gradient produces a metallicity of about $[{\rm Fe/H}] = -0.1$, appropriate for nearby, local stars (Allende Prieto et al. 2004). At a height of $\sim$2 kpc (the maximum height probed by this study), the metallicity is $[{\rm Fe/H}] \sim -0.65$, consistent with measured distributions (Ivezić et al. 2008). The actual metallicity distribution is probably more complex, but given the uncertainties associated with the effects of metallicity on M dwarfs, adopting a more complex description is not justified. The correction to the absolute magnitude, ΔM_r, measured from F and G stars in clusters of known metallicity and distance (Ivezić et al. 2008) is given by

$$\Delta M_r = -0.10920 - 1.11[{\rm Fe/H}] - 0.18[{\rm Fe/H}]^2. \qquad (10)$$

Substituting Equation (9) into Equation (10) yields a quadratic equation for ΔM_r in Galactic height. After initially assigning absolute magnitudes and distances with the CMRs appropriate for nearby stars, each star's estimated height above the plane, $Z_{\rm ini}$, was computed. This is related to the star's actual height, $Z_{\rm true}$, through the following equation:

$$Z_{\rm true} = Z_{\rm ini} 10^{\frac{-\Delta M_r(Z_{\rm true})}{5}}. \qquad (11)$$

A star's true height above the plane was calculated by finding the root of this nonlinear equation. Since ΔM_r is a positive value, the actual distance from the Galactic plane, $Z_{\rm true}$, is smaller than the initial estimate, $Z_{\rm ini}$. As explained above, this effect becomes important at larger distances, moving stars inward and decreasing the density gradient. Thus, if metallicity effects are neglected, the scale heights and lengths are overestimated.
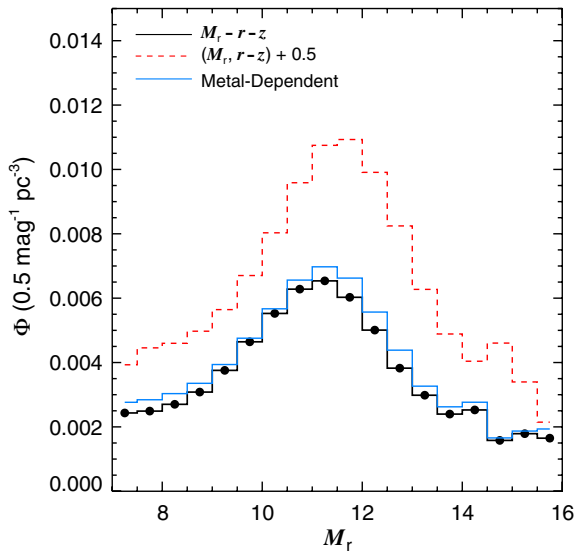
Figure 16. Differences in the LF induced by metallicity gradients, along with the raw LF (black line). The red histogram corresponds to the extreme limit, where all stars are metal-poor ([Fe/H] ~ -0.65). The blue histogram shows the effect of the metallicity gradient from Equation (9).

(A color version of this figure is available in the online journal.)

Figure 17. Systematic effect of extinction on the raw LF. When no extinction correction is applied (open squares), distant stars act to inflate the local densities of the brightest stars, compared to the fiducial case (filled circles). At fainter luminosities, this effect becomes less important.

In Figure 16, the systematic effects of metallicity-dependent CMRs are shown. The first is the extreme limit, shown as the red histogram, where all stars in the sample have an [Fe/H] ~ -0.65, corresponding to a ΔM_r of roughly 0.5 mag. All of the stars in the sample are shifted to smaller distances, greatly enhancing the local density. This limit is probably not realistic, as prior LF studies (e.g., Reid & Gizis 1997; Cruz et al. 2007) would have demonstrated similar behavior. The effect of the metallicity gradient given in Equation (9) is shown with the solid blue line. Note that local densities are increased, since more stars are shifted to smaller distances.

5.2. Systematic CMRs: Extinction

The extinction and reddening corrections applied to SDSS photometry are derived from the Schlegel et al. (1998) dust maps and an assumed dust law of $R_V = 3.1$ (Cardelli et al. 1989). The median extinction in the sample is $A_r = 0.09$, while 95% of the sample has $A_r < 0.41$. Typical absolute magnitude differences due to reddening range up to $\sim$1 mag, producing distance corrections of $\sim$40 pc, enough to move stars between adjacent R, Z bins and absolute magnitude bins. This effect introduces strong covariances between adjacent luminosity bins, and implies that the final LF depends on the assumed extinction law. Most of the stars in our sample lie beyond the local dust column, and the full correction is probably appropriate (Marshall et al. 2006). To bracket the effects of extinction on our analysis, two LFs were computed. The first is the $(M_r, r-z)$ LF, which employs the entire extinction correction. The second uses the same CMR, but without correcting for extinction. The two LFs are compared in Figure 17. When the extinction correction is neglected, stellar distances are underestimated, which increases the local density. This effect is most pronounced for larger luminosities. The dominant effect in this case is not the attenuation of light due to extinction, but rather the reddening of stars, which causes the stellar absolute magnitudes to be underestimated.
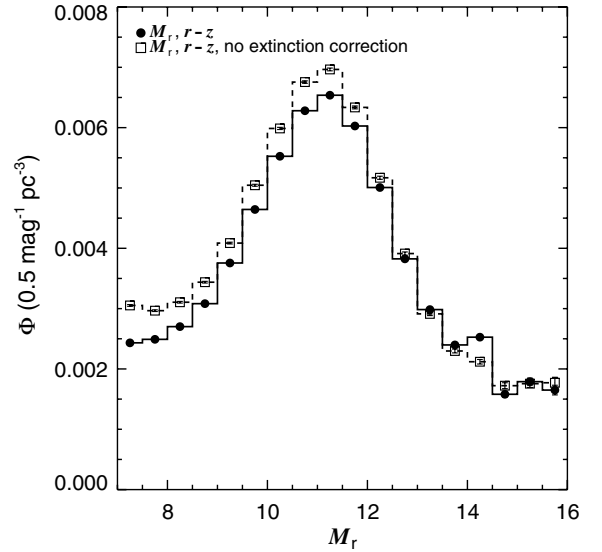
5.3. Systematic Uncertainties

The statistical error in a given LF bin is quite small, typically $\lesssim 0.1\%$, and does not represent a major source of uncertainty in this analysis. The assumed CMR dominates the systematic uncertainty, affecting the shape of the LF and resulting MF. To quantify the systematic uncertainty in the LF and GS, the following procedure was employed. The LF was computed five times using different CMRs: the $(M_r, r-z)$ and $(M_r, r-i)$ CMRs with and without metallicity corrections, and the $(M_r, r-z)$ CMR without correcting for Galactic extinction. The LFs measured by each CMR are plotted in Figure 18, along with the unweighted mean of the five LF determinations. The uncertainty in a given LF mag bin was set by the maximum and minimum of the five test cases, often resulting in asymmetric error bars. This uncertainty was propagated through the entire analysis pipeline using three LFs: the mean, the "maximum" LF, corresponding to the maximum Φ in each magnitude bin, and the "minimum" LF, corresponding to the lowest Φ value. We adopted the mean LF as the observed system LF and proceeded to correct it for the effects of Malmquist bias and binarity, as described below.

5.4. Monte Carlo Models: Malmquist Bias

Malmquist bias (Malmquist 1936) arises in flux-limited surveys (such as SDSS), when distant stars with brighter absolute magnitudes (either intrinsically, from the width of the main sequence, or artificially, due to measurement error) scatter into the survey volume. These stars have their absolute magnitudes systematically overestimated (i.e., they are assigned fainter absolute magnitudes than they actually possess), which leads to underestimated intrinsic luminosities. Thus, their distances will be systematically underestimated. This effect artificially shrinks the observed scale heights and inflates the measured LF densities. Assuming a Gaussian distribution about a "true" mean absolute magnitude $M_\circ$, classical Malmquist bias is given by

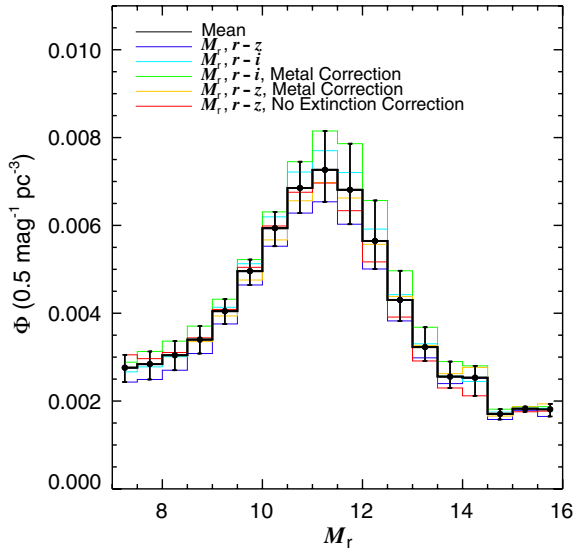$$\bar{M}(m) = M_\circ - \frac{\sigma^2}{\log e} \frac{dA(m)}{dm}, \qquad (12)$$

Figure 18. Mean observed system LF, derived from five different CMRs. Each CMR is described in the legend. The uncertainty in a given LF bin is set by the full range spanned by the five different LFs.

(A color version of this figure is available in the online journal.)

Figure 19. Effects of Malmquist bias (orange and blue filled circles), unresolved binarity (black), and GS on the survey. The mean observed LF is larger than the corrected LF at most bins. The largest effects are seen for the brightest stars, which are subject to the largest shifts due to a change in the thin disk scale height. The difference between the orange and blue LFs demonstrates the sensitivity of the Malmquist correction to the assumed scatter in the main sequence. The binary correction becomes relatively more important at fainter absolute magnitudes. The LF from Jurić et al. (2008, open squares) is shown for comparison to our raw system LF. They did not probe faint absolute magnitudes, employed a different CMR, and did not correct their densities for Malmquist bias, which accounts for the offsets between their LF and ours.

(A color version of this figure is available in the online journal.)

where σ is the spread in the main sequence (or CMR), $dA(m)/dm$ is the slope of the star counts as a function of apparent magnitude m, and $\bar{M}(m)$ is the observed mean absolute magnitude. Qualitatively, $\bar{M}(m)$ is always less than $M_\circ$ (assuming $dA(m)/dm$ is positive), meaning that the observed absolute magnitude distribution is skewed toward more luminous objects.

Malmquist bias effects were quantified by including dispersions in absolute magnitude of $\sigma_{M_r} = 0.3$ and $\sigma_{M_r} = 0.5$ mag and a color dispersion of $\sigma_{r-z, r-i} = 0.05$ mag. These values were chosen to bracket the observed scatter in the color–magnitude diagrams (see Table 4). The LF measured with the Malmquist bias model is shown in Figure 19. The correction is important for most of the stars in the sample, especially the brightest stars ($M_r < 10$). Stars at this magnitude and color ($r - i \sim 0.5$, $r - z \sim 1$; see Figure 4) are very common in the SDSS sample because they span a larger volume than lower-luminosity stars. Thus, they are more susceptible to having over-luminous stars scattered into their absolute magnitude bins. However, the dominant factor that produced the differences between the raw and corrected LFs was the value of the thin disk scale height.

5.5. Monte Carlo Models: Unresolved Binarity

For all but the widest pairs, binaries in our sample will masquerade as a single star. The unresolved duo will be over-luminous at a given color, leading to an underestimate of its distance. This compresses the density maps, leading to decreased scale heights and lengths, as binary systems are assigned smaller distances appropriate to single stars.

Currently, the parameter space that describes M dwarf binaries, binary fraction, mass ratio, and average separation, is not well constrained. However, there are general trends that are useful for modeling their gross properties. First, the binary fraction (f_b) seems to steadily decline from $\sim$50% at F and G stars (Duquennoy & Mayor 1991) to about 30% for M dwarfs (Fischer & Marcy 1992; Delfosse et al. 2004; Lada 2006; Burgasser et al. 2007). Next, the mass ratio distribution becomes increasingly peaked toward unity at lower masses. That is, F and
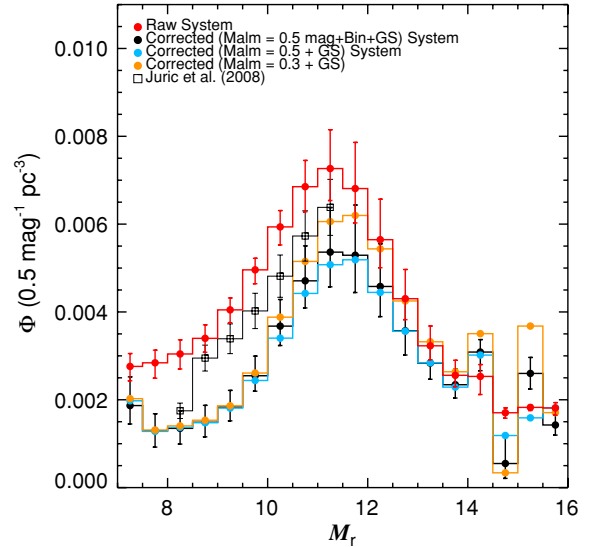
G stars are more likely to have a companion from a wide range of masses, while M dwarfs are commonly found with a companion of nearly the same mass, when the M dwarf is the primary (warmer) star (Burgasser et al. 2007). The average separation distribution is not well known, but many companions are found with separations of $\sim$10–30 AU (Fischer & Marcy 1992), while very low mass stars have smaller average separations (Burgasser et al. 2007). At the typical distances probed by the SDSS sample (hundreds of pc) these binary systems would be unresolved by SDSS imaging with an average PSF width of $1\farcs4$ in r.

We introduced binaries into our simulations with four different binary fraction prescriptions. The first three ($f_b = 30\%, 40\%$, and 50%) are independent of primary star mass. The fourth binary fraction follows the methodology of Covey et al. (2008) and is a primary-star mass–dependent binary fraction, given by

$$f_b(\mathcal{M}_p) = 0.45 - \frac{0.7 - \mathcal{M}_p}{4}, \qquad (13)$$

where $\mathcal{M}_p$ is the mass of the primary star, estimated using the Delfosse et al. (2000) mass–luminosity relations. This linear equation reflects the crude observational properties described above for stars with $\mathcal{M}_p < 0.7\,\mathcal{M}_\odot$. Near $1\,\mathcal{M}_\odot$, the binary fraction is $\sim$50%, while at smaller masses, the binary fraction falls to $\sim$30%. Secondary stars are forced to be less massive than their primaries. This is the only constraint on the mass ratio distribution.

An iterative process, similar to that described in Covey et al. (2008), is employed to estimate the binary-star population. First, the mean observed LF from Figure 18 is input as a primary-star LF (PSLF). A mock stellar catalog is drawn from the PSLF, and binary stars are generated with the prescriptions described above. Next, the flux from each pair is merged, and new
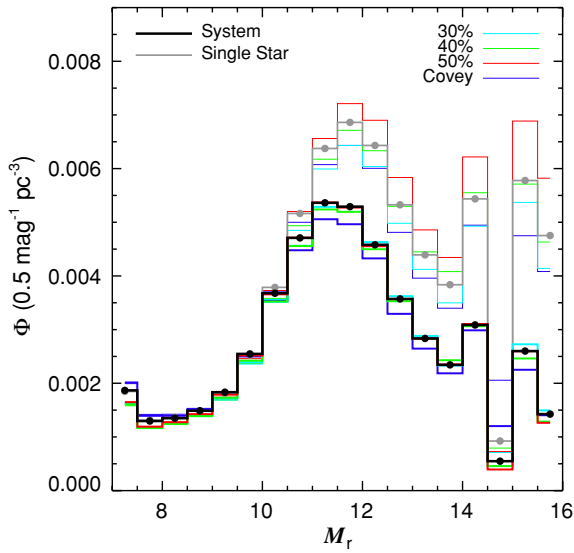
Figure 20. System and single-star M_r LFs for our four different binary prescriptions. The spread between prescriptions in each bin is used to calculate the final uncertainty in the system and single-star LFs.

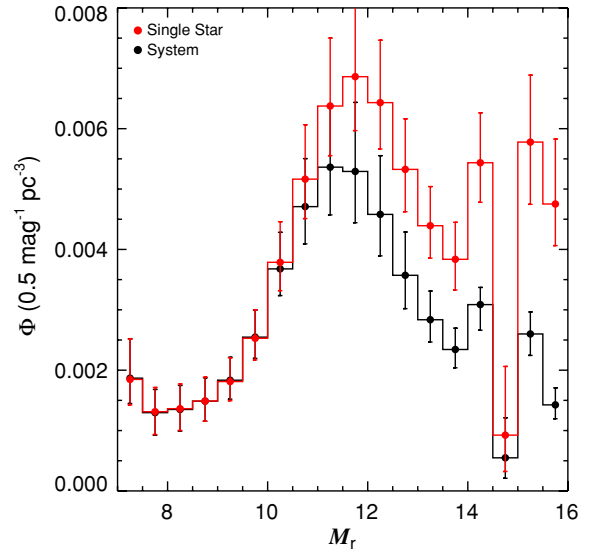(A color version of this figure is available in the online journal.)

Figure 21. Single-star (red filled circles) and system (black filled circles) LFs. Note that the major differences between our system and single-star LFs occur at low luminosities, since low-mass stars can be companions to stars of any higher mass, including masses above those sampled here.

(A color version of this figure is available in the online journal.)

colors and brightnesses are calculated for each system. Scatter is introduced in color and absolute magnitude, as described in Section 5.4. The stellar catalog is analyzed with the same pipeline as the data, and the output model LF is compared to the observed LF. The input PSLF is then tweaked according to the differences between the observed system LF and the model system LF. This loop is repeated until the artificial system LF matches the observed system LF. Note that the GS parameters are also adjusted during this process, and the bias-corrected values are given in Table 6. The thin disk scale height, which has a strong effect on the derived LF, is in very good agreement with previous values. As the measured thin disk scale height increases, the density gradients decrease, and a smaller local density is needed to explain distant structures. This change is most pronounced at the bright end, where the majority of the stars are many thin disk scale heights away from the Sun (see Figure 19). The preferred model thin disk and thick disk scale lengths were found to be similar. This is most likely due to the limited radial extent of the survey compared to their typical scale lengths. Upcoming IR surveys of disk stars, such as APOGEE (Allende Prieto et al. 2008), should provide more accurate estimates of these parameters.

SDSS observations form a sensitive probe of the thin disk and thick disk scale heights, since the survey focused mainly on the northern Galactic cap. Our estimates suggest a larger thick disk scale height and smaller thick disk fraction than recent studies (e.g., Siegel et al. 2002; Jurić et al. 2008). However, these two parameters are highly degenerate (see Figure 1 of Siegel et al. 2002). In particular, the differences between our investigation and the Jurić et al. (2008) study highlight the sensitivity of these parameters to the assumed CMR and density profiles, as they included a halo in their study and we did not. The Jurić et al. (2008) study sampled larger distances than our work, which may affect the resulting Galactic parameters. However, the smaller normalization found in our study is in agreement with recent results from a kinematic analysis of nearby M dwarfs with SDSS spectroscopy (J. S. Pineda et al. 2010, in preparation). They find a relative normalization of ~5%, similar to the present investigation. The discrepancy in scale height

highlights the need for additional investigations into the thick disk and suggests that future investigations should be presented in terms of stellar mass contained in the thick disk, not scale height and normalization.

The iterative process described above accounts for binary stars in the sample and allows us to compare the system LF and single-star LF in Figure 20. Most observed LFs are system LFs, except for the local volume-limited surveys. However, most theoretical investigations into the IMF predict the form of the single-star MF. Note that for all binary prescriptions, the largest differences between the two LFs are seen at the faintest M_r, since the lowest-luminosity stars are most easily hidden in binary systems.

6. RESULTS: LUMINOSITY FUNCTION

The final adopted system and single-star M_r LFs are presented in Figure 21. The LFs were corrected for unresolved binarity and Malmquist bias. The uncertainty in each bin is computed from the spread due to CMR differences, binary prescriptions, and Malmquist corrections. The mean LFs and uncertainties are listed in Tables 7 and 8. The differences between the single and system LFs are discussed below and compared to previous studies in both M_r and M_J.

6.1. Single-star versus System Luminosity Functions

Figure 21 demonstrates a clear difference between the single-star LF and the system LF. The single-star LF rises above the system LF near the peak at $M_r \sim 11$ (or a spectral type ~M4) and maintains a density about twice that of the system LF.[13] This implies that lower-luminosity stars are easily hidden in binary systems, but isolated low-luminosity systems

---

[13] We note that the differences between our system and single-star LFs disagree considerably with those reported by Covey et al. (2008). These differences were investigated, and the Covey et al. (2008) binary corrections were found to be erroneous, with companion stars sampled from the MF convolved with the full sample volume, which is inappropriate for companion stars. The authors regret the error.

Table 7
Final System M_r Luminosity Function

M_r Bin	Φ_{Mean}	Φ_{Max}	Φ_{Min}
7.25	1.87	2.52	1.45
7.75	1.30	1.68	0.92
8.25	1.35	1.75	0.99
8.75	1.49	1.87	1.16
9.25	1.83	2.21	1.52
9.75	2.55	2.99	2.20
10.25	3.68	4.28	3.24
10.75	4.71	5.50	4.09
11.25	5.36	6.38	4.57
11.75	5.29	6.44	4.44
12.25	4.58	5.55	3.89
12.75	3.57	4.29	3.02
13.25	2.84	3.31	2.47
13.75	2.34	2.70	2.04
14.25	3.09	3.37	2.66
14.75	0.55	1.21	0.21
15.25	2.60	2.96	2.24
15.75	1.43	1.71	1.20

Note. Densities are reported in units of (stars pc^{-3} 0.5 mag^{-1}) $\times 10^{-3}$.

Table 8
Final Single M_r Luminosity Function

M_r Bin	Φ_{Mean}	Φ_{Max}	Φ_{Min}
7.25	1.85	2.51	1.43
7.75	1.31	1.71	0.93
8.25	1.36	1.77	1.00
8.75	1.49	1.89	1.15
9.25	1.81	2.21	1.49
9.75	2.53	3.00	2.17
10.25	3.79	4.46	3.32
10.75	5.16	6.06	4.51
11.25	6.38	7.50	5.55
11.75	6.86	8.10	5.97
12.25	6.43	7.47	5.66
12.75	5.33	6.16	4.62
13.25	4.39	5.04	3.86
13.75	3.84	4.45	3.33
14.25	5.44	6.26	4.78
14.75	0.92	2.06	0.32
15.25	5.78	6.89	4.75
15.75	4.75	5.83	4.06

Note. Densities are reported in units of (stars pc^{-3} 0.5 mag^{-1}) $\times 10^{-3}$.

Table 9
System M_J Luminosity Function

M_J Bin	Φ_{Mean}	Φ_{Max}	Φ_{Min}
5.25	1.69	2.24	1.27
5.75	1.73	2.24	1.25
6.25	2.31	2.91	1.79
6.75	3.72	4.41	3.16
7.25	6.30	7.35	5.53
7.75	8.10	9.60	6.93
8.25	7.71	9.37	6.50
8.75	5.82	6.99	4.92
9.25	4.48	5.19	3.90
9.75	4.04	5.03	3.22

Note. Densities are reported in units of (stars pc^{-3} 0.5 mag^{-1}) $\times 10^{-3}$.

Table 10
Single-star M_J Luminosity Function

M_J Bin	Φ_{Mean}	Φ_{Max}	Φ_{Min}
5.25	1.68	2.25	1.26
5.75	1.75	2.28	1.27
6.25	2.31	2.93	1.79
6.75	3.69	4.41	3.12
7.25	6.60	7.77	5.78
7.75	9.50	11.17	8.27
8.25	10.26	12.04	8.96
8.75	8.60	9.95	7.48
9.25	7.14	8.23	6.22
9.75	7.08	9.16	5.73

Note. Densities are reported in units of (stars pc^{-3} 0.5 mag^{-1}) $\times 10^{-3}$.

SDSS observations, over different color ranges. Figure 19 compares the M_r system LF determined here to the "joint fit, bright parallax" results of Jurić et al. (2008, their Table 3), assuming 10% error bars. The two raw system LFs broadly agree statistically, although the Jurić et al. (2008) work only probes to $M_r \sim 11$, due to their red limit of $r - i \sim 1.4$. We compare system LFs, since the Jurić et al. (2008) study did not explicitly compute an SSLF and their reported LF was not corrected for Malmquist bias.

6.3. M_J LF

We next converted M_r to M_J using relations derived from the calibration sample described in Bochanski (2008). The J filter has traditionally been used as a tracer of mass (Delfosse et al. 2000) and bolometric luminosity (Golimowski et al. 2004) in low-mass stars, since it samples the spectral energy distribution (SED) near its peak. The largest field LF investigation to date, Covey et al. (2008), determined the J-band LF from $M_J = 4$ to $M_J = 12$. In Figure 22, our transformed system M_J LF (given in Table 9) is plotted with the M_J LF from Covey et al. (2008). The shape of these two LFs agrees quite well, both peaking near $M_J = 8$, although there appears to be a systematic offset, in that our M_J LF is consistently lower than the one from the Covey et al. (2008) study. This is most likely due to the different CMRs employed by the two studies. Covey et al. (2008) used an $(M_i, i - J)$ CMR, as opposed to the various CMRs employed in the current study.

Figure 22 also compares our single-star M_J LF (Table 10) to the LF of primaries and secondaries, first measured by Reid & Gizis (1997) and updated by Cruz et al. (2007). These stars are drawn from a volume-complete sample with $d < 8$ pc. A
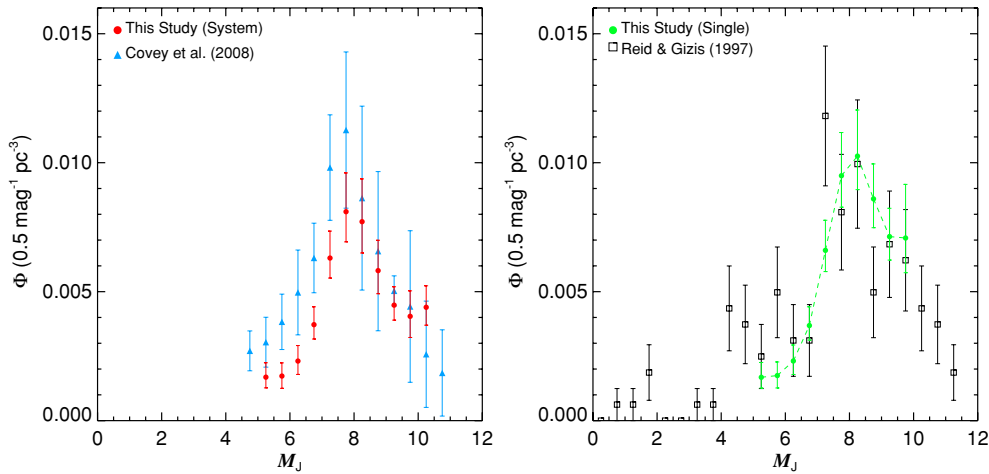
are intrinsically rare. The agreement between the system and single-star LFs at high luminosities is a byproduct of our binary prescription, which enforced that a secondary be less massive than its primary-star counterpart. Since our LF does not extend to higher masses (G and K stars), we may be missing some secondary companions to these stars, which would inflate the single-star LF at high luminosities. However, only ~700,000 G dwarfs are present in the volume probed by this study. Even if all of these stars harbored an M-dwarf binary companion, the resulting differences in a given bin would only be a fraction of a percent.

6.2. M_r LF

Since many traditional LF studies have not employed the r band, our ability to compare our work to previous results is hampered. The most extensive study of the M_r LF was conducted by Jurić et al. (2008), using 48 million photometric

Figure 22. Left panel: M_J system LF. We compare our system LF (red filled circles) to the system LF measured by Covey et al. (2008, blue triangles). Our system LF and the Covey et al. (2008) results agree reasonably well. Right panel: M_J single-star LF. We compare our LF for single stars (green filled circles and dashed line) compared to the single-star LF measured by Reid et al. (2002, open squares). The single-star LFs also agree within the uncertainties, except for a few bins, resolving previous discrepancies between photometric and volume-complete samples.

(A color version of this figure is available in the online journal.)

total of 146 stars in 103 systems are found within this limit. The distances for the stars in this volume-complete sample are primarily found from trigonometric parallaxes, with <5% of the stellar distances estimated by spectral type. There is reasonable agreement between our M_J LF and the LF from the volume-complete sample, within the estimated uncertainties, indicating that the photometric and volume-complete methods now give similar results. Furthermore, it indicates that our assumed CMRs are valid for local, low-mass stars. Finally, the agreement between the single-star LFs validates our assumed corrections for unresolved binarity.

7. RESULTS: MASS FUNCTION

The MF was calculated from the M_J LFs and the mass–luminosity (M_J) relation from Delfosse et al. (2000). We computed both a single-star MF and a system MF. As discussed in Covey et al. (2008), some past discrepancies between MFs are probably due to comparing analytic fits and the actual MF data. This effect is discussed below, where we compare our results to available MF data from nearby (e.g., Reid & Gizis 1997) and distant (e.g., Zheng et al. 2001) samples. We also compare our analytic fits to seminal IMF studies.

The single-star and system MFs are shown in Figure 23. As seen in the LFs, there is agreement between the two relations at higher masses. At masses less than 0.5 $\mathcal{M}_\odot$, the shapes of the MFs are roughly equivalent, but the single-star density is roughly twice that of the systems. We note a small possible correction to the lowest-mass bin ($\log \mathcal{M}/\mathcal{M}_\odot = -0.95$). At these masses, young brown dwarfs, with ages less than 1 Gyr and masses near $\mathcal{M} \sim 0.075\ \mathcal{M}_\odot$ will have luminosities similar to late-type M dwarfs. Since these objects are not stellar, they should be removed from our MF. Assuming a constant star formation rate, Chabrier (2003a) estimated that brown dwarfs contribute ~10% of the observed densities at the faintest absolute magnitudes (or lowest masses). Recent studies of nearby, young M dwarfs (e.g., Shkolnik et al. 2009) show that ~10% have ages less than 300 Myr, further supporting the presence of young brown dwarfs in our sample. Thus, a correction of 10% to the lowest-mass bin would account for young brown dwarfs (see Figure 23). We do not apply the correction, but include its impact on the uncertainty of the last MF bin.
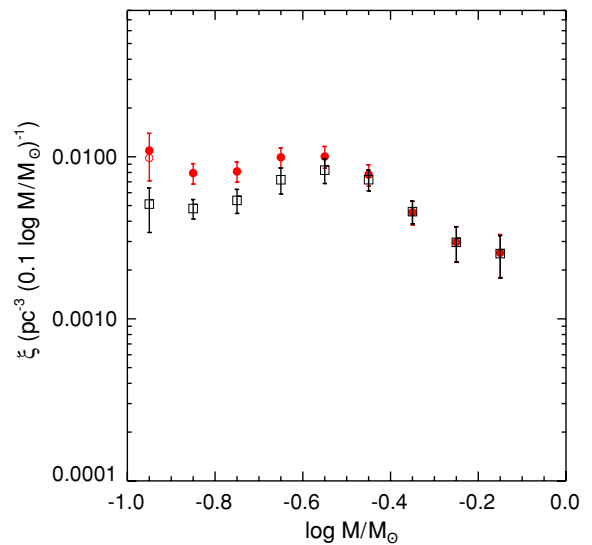

Figure 23. Single-star MF (red filled circles) and system MF (open squares) for this study. Note that the largest differences between the two MFs occur at smaller masses, since low-mass stars are easily obscured in binary systems with a higher-mass primary. The possible correction for young brown dwarfs discussed in Section 7 is shown as an open circle in the single-star MF.

(A color version of this figure is available in the online journal.)

In Figures 24 and 25, we display the lognormal and broken power-law fits to the system and single-star MFs. While the broken power law is preferred by many observers (Covey et al. 2008; Kroupa 2002), the lognormal formalism has been popularized by some theorists (e.g., Padoan et al. 1997; Hennebelle & Chabrier 2008). Our MF data are best fitted by a lognormal distribution, as confirmed by an f test. We suggest using the lognormal form when comparing to previous MF fits, but stress that comparisons using the actual MF data (Tables 11 and 12) are preferred.

The system MF is compared to the pencil-beam survey of Zheng et al. (2001) MF in Figure 24. Their data were acquired with the *HST*, and the stars in their sample are at distances similar to this study. The Zheng et al. (2001) study sparked some discussion in the literature (e.g., Chabrier 2003a, 2003b), as their results differed dramatically from the nearby star
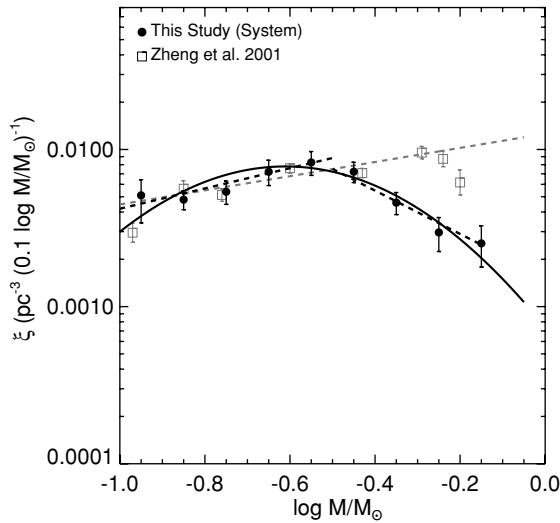
Figure 24. System MF (filled circles), along with broken power-law (dashed line) and lognormal (dot-dashed line) fits. The power-law break occurs near 0.3 $\mathcal{M}_\odot$. The parameters of both fits are found in Table 13. The MF data (open squares) and power-law fit from Zheng et al. (2001, light dashed line) are also shown. The agreement between our data and the Zheng et al. (2001) data is good at lower masses, but the data diverge at higher masses.
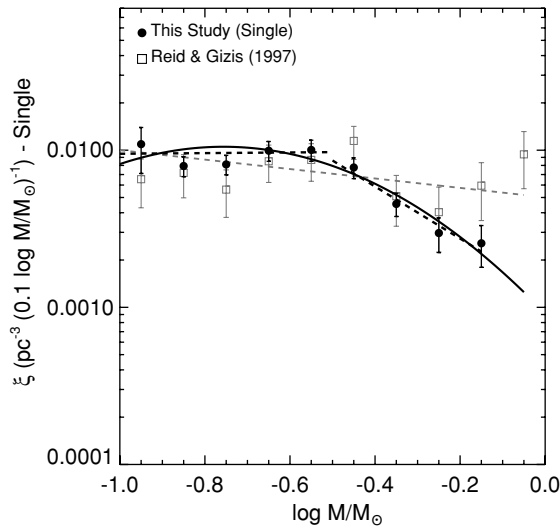

Figure 25. Single-star MF (filled circles). We fit this distribution with a broken power law (dashed line) and a lognormal distribution (dot-dashed line). The parameters of these fits are found in Table 14. The MF data (open squares) and single power-law fit from Reid & Gizis (1997, light dashed line) are also shown. The data are in reasonable agreement, with discrepancies larger than the error bars in only two bins.

sample (e.g., Reid & Gizis 1997). The proposed solution was unresolved binarity. Binary systems would be resolved easily at small distances, but not at the larger distances probed by the *HST* sample. We compare our system MF to the Zheng et al. (2001) sample and find agreement over a large range of masses ($\mathcal{M} < 0.4\,\mathcal{M}_\odot$). At larger masses ($\mathcal{M} \sim 0.4\,\mathcal{M}_\odot$), the MFs diverge. This can most likely be attributed to differing CMRs, in particular differences in the corrections for stellar metallicity gradients.

Our single-star MF is compared to the nearby star sample (Reid & Gizis 1997) in Figure 25. The MFs agree remarkably well, with discrepancies in only two bins (likely the result of small numbers in the nearby star sample). This indicates that our CMRs and methodology are valid, since the output densities are in agreement. It suggests that our binary corrections are

Table 11
System Mass Function

log ($\mathcal{M}/\mathcal{M}_\odot$)	ξ_{Mean}	ξ_{Max}	ξ_{Min}
−0.15	2.53	3.26	1.79
−0.25	2.96	3.69	2.24
−0.35	4.59	5.32	3.85
−0.45	7.22	8.28	6.15
−0.55	8.27	9.70	6.84
−0.65	7.21	8.53	5.89
−0.75	5.38	6.29	4.47
−0.85	4.79	5.45	4.14
−0.95	5.11	6.42	3.41

Note. Densities are reported in units of (stars pc^{-3} 0.1 log M^{-1}) $\times 10^{-3}$.

Table 12
Single-star Mass Function

log ($\mathcal{M}/\mathcal{M}_\odot$)	ξ_{Mean}	ξ_{Max}	ξ_{Min}
−0.15	2.56	3.31	1.80
−0.25	2.97	3.71	2.23
−0.35	4.55	5.31	3.79
−0.45	7.76	8.93	6.59
−0.55	10.04	11.58	8.50
−0.65	9.93	11.36	8.50
−0.75	8.12	9.27	6.97
−0.85	7.93	9.08	6.78
−0.95	10.92	13.95	7.11

Note. Densities are reported in units of (stars pc^{-3} 0.1 log M^{-1}) $\times 10^{-3}$.

reasonable, as both our system and single-star MFs agree with previous results. Moreover, the discrepancy between the Reid & Gizis (1997) and Zheng et al. (2001) MFs can be attributed to unresolved binarity. The Reid & Gizis (1997) MF results present a single-star MF, while the Zheng et al. (2001) MF is a system MF.

We compare our single-star LF to seminal IMF analytic fits in Figure 26 (see Table 1). While we advocate the comparison of MF data whenever possible (as discussed in Covey et al. 2008), it is informative to compare our results to these studies. The Kroupa (2002) and Chabrier (2003a) studies demonstrate the best agreement with our data at masses $\mathcal{M} < 0.4\,\mathcal{M}_\odot$, but diverge at higher masses, predicting larger space densities than we infer here. The disagreement of the Miller & Scalo (1979) MF with the other three MFs suggests an issue with their normalization.

7.1. The IMF in other Mass Regimes

A single analytic description of the IMF over a wide range in mass may not be appropriate. Figure 27 shows the derived MFs from this study, and those from the Reid & Gizis (1997) sample and the Pleiades (Moraux et al. 2004). The lognormal fit from this study is extended to higher masses, and it clearly fails to match the Pleiades MF. Therefore, it is very important to only use the analytic fits over the mass ranges where they are appropriate. Extending analytic fits beyond their quoted bounds can result in significant inaccuracies in the predicted number of stars.

7.2. Theoretical Implications of the IMF

Any successful model of star formation must accurately predict the IMF. The measured field MF traces the IMF of low-mass stars averaged over the star formation history of the Milky Way. Thus, the field MF is not a useful tool for investigating changes in the IMF due to physical conditions in the star-forming
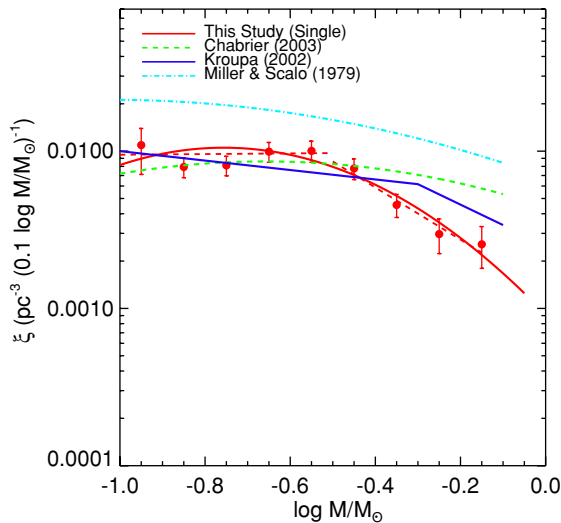
Figure 26. Shown are the MF data and best lognormal fit from this study (solid circles and red line), along with the analytic MF fits of Chabrier (2003a, green dashed line), Kroupa (2002, dark blue dash-dot-dot-dotted line), and Miller & Scalo (1979, light blue dash-dotted line). We stress that comparing actual MF data is more valid than comparing analytic fits.

(A color version of this figure is available in the online journal.)

Figure 27. Shown are the single-star MF and best lognormal fit from this study (red filled circles and solid line), the Reid & Gizis (1997, open squares), MF (open squares), and the Pleiades MF Moraux et al. (2004, green triangles). The best fit extrapolated from our study systematically under-predicts the density at masses outside the bounds of our data.

(A color version of this figure is available in the online journal.)

regions, such as density or metallicity. However, it does lend insight into the dominant physical processes that shape the IMF. Recent theoretical investigations (see Elmegreen 2007, and references therein) have mainly focused on three major mechanisms that would shape the low-mass IMF: turbulent fragmentation, competitive accretion and ejection, and thermal cooling arguments.

Turbulent fragmentation occurs when supersonic shocks compress the molecular gas (Larson 1981; Padoan et al. 2001). Multiple shocks produce filaments within the gas, with properties tied to the shock properties. Clumps then form along these filaments and collapse ensues. In general, the shape of the IMF depends on the Mach number and power spectrum of shock velocities (Ballesteros-Paredes et al. 2006; Goodwin et al. 2006) and the molecular cloud density (Padoan & Nordlund 2002). Turbulence readily produces a clump distribution similar to the ubiquitous Salpeter IMF at high masses ($>1\,\mathcal{M}_\odot$). However, the flattening at lower masses is reproduced if only a fraction of clumps are dense enough to form stars (Moraux et al. 2007).

An alternative model to turbulent fragmentation is accretion and ejection (Bate & Bonnell 2005). Briefly, small cores form near the opacity limit ($\sim 0.003\,\mathcal{M}_\odot$), which is set by cloud composition, density, and temperature. These clumps proceed to accrete nearby gas. Massive stars form near the center of the cloud's gravitational potential, thus having access to a larger gas reservoir. Accretion ends when the nascent gas is consumed or the accreting object is ejected via dynamical interactions. The characteristic mass is set by the accretion rate and the typical timescale for ejection, with more dense star-forming environments producing more low-mass stars. This method has fallen out of favor recently, as brown dwarfs have been identified in weakly bound binaries (Luhman 2004b; Luhman et al. 2009), which should be destroyed if ejection is a dominant mechanism. Furthermore, if ejection is important, the spatial density of brown dwarfs should be higher near the outskirts of a cluster compared to stars, and this is not observed in Taurus (Luhman 2004a, 2006) or Chamaeleon (Joergens 2006).

Larson (2005) suggested that thermal cooling arguments are also important in star formation. This argument has gained some
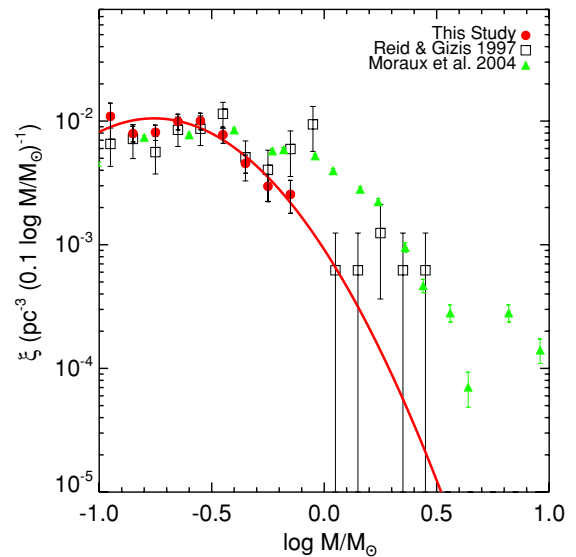
popularity, as it predicts a relative insensitivity of the IMF to initial conditions, which is supported by many observations (e.g., Kroupa 2002; Moraux et al. 2007; Bastian et al. 2010; and references therein). This insensitivity is due to changes in the cooling rate with density. At low densities, cooling is controlled by atomic and molecular transitions, while at higher densities, the gas is coupled with dust grains, and these dust grains dominate the cooling. The result is an equation of state with cooling at low densities and a slight heating term at high densities. This equation of state serves as a funneling mechanism and imprints a characteristic mass on the star formation process, with little sensitivity to the initial conditions.

The general shape of the IMF has been predicted by star formation theories that account for all of these effects (Chabrier 2003a, 2005). In particular, the high-mass IMF is regulated by the power spectrum of the turbulent flows (Padoan & Nordlund 2002; Hennebelle & Chabrier 2009) and is probably affected by the coagulation of less massive cores, while the flatter, low-mass distribution can be linked to the dispersions in gas density and temperatures (Moraux et al. 2007; Bonnell et al. 2006). As the IMF reported in this study is an average over the star formation history of the Milky Way, changes in the characteristic shape of the IMF cannot be recovered. However, our observational IMF can rule out star formation theories that do not show a flattening at low masses, with a characteristic mass $\sim 0.2\,\mathcal{M}_\odot$. Recent numerical simulations have shown favorable agreement with our results (Bate 2009); however, most numerical simulations of star formation are restricted in sample size and suffer significant Poisson uncertainties. Analytical investigations of the IMF (Hennebelle & Chabrier 2008) are also showing promising results, reproducing characteristic masses $\sim 0.3\,\mathcal{M}_\odot$ and lognormal distributions in the low-mass regime.

8. CONCLUSIONS

We have assembled the largest set of photometric observations of M dwarfs to date and used it to study the low-mass stellar luminosity and MFs. Previous studies were limited by

Table 13
System Mass Function Analytic Fits

Form	Mass Range	Parameter
lognormal	$-1.0 < \log \mathcal{M}/\mathcal{M}_\odot < -0.1$	$C_\circ = 0.008 \pm 0.001$
		$\mathcal{M}_\circ = 0.25 \pm 0.01$
		$\sigma = 0.28 \pm 0.02$
Broken power law (low mass)	$0.1\,\mathcal{M}_\odot < \mathcal{M} < 0.32\,\mathcal{M}_\odot$	$\alpha = 0.35 \pm 0.07$
Broken power law (high mass)	$0.32\,\mathcal{M}_\odot < \mathcal{M} < 0.8\,\mathcal{M}_\odot$	$\alpha = 2.38 \pm 0.05$

Note. We use the form $\psi(\mathcal{M}) = C_\circ e^{\frac{(\log \mathcal{M} - \log \mathcal{M}_\circ)^2}{2\sigma^2}}$ for the lognormal fit and $\psi(\mathcal{M}) \propto \mathcal{M}^{-\alpha}$ for the power-law fit.

Table 14
Single Mass Function Analytic Fits

Form	Mass Range	Parameter
lognormal	$-1.0 < \log \mathcal{M}/\mathcal{M}_\odot < -0.1$	$C_\circ = 0.011 \pm 0.002$
		$\mathcal{M}_\circ = 0.18 \pm 0.02$
		$\sigma = 0.34 \pm 0.05$
Broken power law (low mass)	$0.1\,\mathcal{M}_\odot < \mathcal{M} < 0.32\,\mathcal{M}_\odot$	$\alpha = 0.98 \pm 0.15$
Broken power law (high mass)	$0.32\,\mathcal{M}_\odot < \mathcal{M} < 0.8\,\mathcal{M}_\odot$	$\alpha = 2.66 \pm 0.10$

sample size, mostly due to the intrinsic faintness of M dwarfs. The precise photometry of the SDSS allowed us to produce a clean, complete sample of M dwarfs, nearly 2 orders of magnitude larger than other studies.

To accurately estimate the brightness and distances to these stars, we constructed new photometric parallax relations from data kindly provided to us prior to publication (D. A. Golimowski et al. 2010, in preparation). These relations were derived from $ugrizJHK_s$ photometry of nearby stars with known trigonometric parallax measurements. We compared our new relations to those previously published for SDSS observations.

We also introduced a method for measuring the LF within large surveys. Previous LF investigations either assumed a Galactic profile (for pencil-beam surveys, such as Zheng et al. 2001) or a constant density (for nearby stars, i.e., Reid & Gizis 1997). However, none of these samples have approached the solid angle or the number of the stars observed in this study. We solved for the LF and GS simultaneously, using a technique similar to Jurić et al. (2008). Our LF is measured in the r band. Using multiple CMRs, we investigated systematic errors in the LF and computed the effects of Malmquist bias, unresolved binarity, and GS changes using MC models. This allowed us to compare our results both to distant LF studies (which sampled mostly the system LF) and nearby star samples (which can resolve single stars in binary systems).

Finally, we computed MFs for single stars and systems. Low-luminosity stars are more common in the single-star MF, since they can be companions to any higher-mass star. We fitted both MFs with a broken power law, a form preferred by Kroupa (2002), and a lognormal distribution, which is favored by Chabrier (2003a). The lognormal distribution at low masses seems to be ubiquitous: it is evident both in the field (this study; Chabrier 2003a) and open clusters, such as Blanco 1 (Moraux et al. 2007), the Pleiades (Moraux et al. 2004), and NGC 6611 (Oliveira et al. 2009). The best fits for this study are reported in Tables 13 and 14. We stress the point first made in Covey et al. (2008) that comparing MF *data* is preferable to comparing analytic fits, since the latter are often heavily swayed by slight discrepancies among the data. We also caution the reader against extrapolating our reported MF beyond 0.1 $\mathcal{M}_\odot < \mathcal{M} < 0.8\,\mathcal{M}_\odot$, the masses that bound our sample. In the future, we plan to investigate the LF in other SDSS bandpasses, such as i and z. Our system and single-star MFs represent the best current values for this important quantity for low-mass stars.

REFERENCES

Abazajian, K. N., et al. 2009, ApJS, 182, 543
Adelman-McCarthy, J. K., et al. 2008, ApJS, 175, 297
Allende Prieto, C., Barklem, P. S., Lambert, D. L., & Cunha, K. 2004, A&A, 420, 183
Allende Prieto, C., et al. 2008, Astron. Nachr., 329, 1018
An, D., et al. 2008, ApJS, 179, 326
Ballesteros-Paredes, J., Gazol, A., Kim, J., Klessen, R. S., Jappsen, A., & Tejero, E. 2006, ApJ, 637, 384
Baraffe, I., Chabrier, G., Allard, F., & Hauschildt, P. H. 1998, A&A, 337, 403
Bastian, N., et al. 2010, ARA&A, in press (arXiv:1001.2965)
Bate, M. R. 2009, MNRAS, 392, 1363
Bate, M. R., & Bonnell, I. A. 2005, MNRAS, 356, 1201
Belokurov, V., et al. 2006, ApJ, 642, L137
Belokurov, V., et al. 2007, ApJ, 654, 897
Binney, J., Gerhard, O., & Spergel, D. 1997, MNRAS, 288, 365
Bochanski, J. J., Munn, J. A., Hawley, S. L., West, A. A., Covey, K. R., & Schneider, D. P. 2007a, AJ, 134, 2418
Bochanski, J. J., West, A. A., Hawley, S. L., & Covey, K. R. 2007b, AJ, 133, 531
Bochanski, J. J., Jr. 2008, PhD thesis, University of Washington
Bonnell, I. A., Clarke, C. J., & Bate, M. R. 2006, MNRAS, 368, 1296
Burgasser, A. J., & Kirkpatrick, J. D. 2006, ApJ, 645, 1485
Burgasser, A. J., Reid, I. N., Siegler, N., Close, L., Allen, P., Lowrance, P., & Gizis, J. 2007, in Protostars and Planets V, ed. B. Reipurth, D. Jewitt, & K. Keil (Tucson, AZ: Univ. Arizona Press), 427
Burgasser, A. J., Vrba, F. J., Lépine, S., Munn, J. A., Luginbuhl, C. B., Henden, A. A., Guetter, H. H., & Canzian, B. C. 2008, ApJ, 672, 1159
Burgasser, A. J., et al. 2002, ApJ, 564, 421
Cardelli, J. A., Clayton, G. C., & Mathis, J. S. 1989, ApJ, 345, 245
Carollo, D., et al. 2007, Nature, 450, 1020
Chabrier, G. 2001, ApJ, 554, 1274
Chabrier, G. 2003a, PASP, 115, 763
Chabrier, G. 2003b, ApJ, 586, L133
Chabrier, G. 2005, in The Initial Mass Function 50 Years Later, ed. E. Corbelli, F. Palla, & H. Zinnecker (Astrophys. Space Sci. Lib. 327; Dordrecht: Springer), 41
Clem, J. L., Vanden Berg, D. A., & Stetson, P. B. 2008, AJ, 135, 682
Cohen, M. 1995, ApJ, 444, 874
Covey, K. R., et al. 2007, AJ, 134, 2398
Covey, K. R., et al. 2008, AJ, 136, 1778
Cruz, K. L., et al. 2007, AJ, 133, 439
Cutri, R. M., et al. 2003, VizieR Online Data Catalog, 2246, 0
Dahn, C. C., Liebert, J., & Harrington, R. S. 1986, AJ, 91, 621
Dahn, C. C., et al. 2002, AJ, 124, 1170
Davenport, J. R. A., Bochanski, J. J., Covey, K. R., Hawley, S. L., West, A. A., & Schneider, D. P. 2007, AJ, 134, 2430
Delfosse, X., Forveille, T., Ségransan, D., Beuzit, J.-L., Udry, S., Perrier, C., & Mayor, M. 2000, A&A, 364, 217
Delfosse, X., et al. 2004, in ASP Conf. Ser. 318, Spectroscopically and Spatially Resolving the Components of the Close Binary Stars, ed. R. W. Hilditch, H. Hensberge, & K. Pavlovski (San Francisco, CA: ASP), 166
Duquennoy, A., & Mayor, M. 1991, A&A, 248, 485
Elmegreen, B. G. 2007, in ASP Conf. Ser. 362, The Seventh Pacific Rim Conference on Stellar Astrophysics, ed. Y. W. Kang et al. (San Francisco, CA: ASP), 269
ESA 1997, VizieR Online Data Catalog, 1239, 0
Fischer, D. A., & Marcy, G. W. 1992, ApJ, 396, 178
Fuchs, B., et al. 2009, AJ, 137, 4149
Fukugita, M., Ichikawa, T., Gunn, J. E., Doi, M., Shimasaku, K., & Schneider, D. P. 1996, AJ, 111, 1748
Giclas, H. L., Burnham, R., & Thomas, N. G. 1971, Lowell Proper Motion Survey Northern Hemisphere. The G Numbered Stars. 8991 Stars Fainter than Magnitude 8 with Motions <0″.6/year (Flagstaff, AZ: Lowell Observatory)
Girardi, L., Grebel, E. K., Odenkirchen, M., & Chiosi, C. 2004, A&A, 422, 205
Gizis, J. E. 1997, AJ, 113, 806
Gliese, W., & Jahreiss, H. 1991, in The Astronomical Data Center CD-ROM: Selected Astronomical Catalogs, Preliminary Version of the Third Catalogue of Nearby Stars, Technical Report, ed. E. Brotzmann & S. E. Gesser (Greenbelt, MD: NASA/Astronomical Data Center)
Golimowski, D. A., et al. 2004, AJ, 127, 3516
Goodwin, S. P., Whitworth, A. P., & Ward-Thompson, D. 2006, A&A, 452, 487
Gould, A., Bahcall, J. N., & Flynn, C. 1996, ApJ, 465, 759
Gould, A., Bahcall, J. N., & Flynn, C. 1997, ApJ, 482, 913
Gunn, J. E., et al. 1998, AJ, 116, 3040

Gunn, J. E., et al. 2006, AJ, 131, 2332
Hanson, R. B. 1979, MNRAS, 186, 875
Hawley, S. L., Gizis, J. E., & Reid, I. N. 1996, AJ, 112, 2799
Hawley, S. L., et al. 2002, AJ, 123, 3409
Hennebelle, P., & Chabrier, G. 2008, ApJ, 684, 395
Hennebelle, P., & Chabrier, G. 2009, ApJ, 702, 1428
Henry, T. J., Kirkpatrick, J. D., & Simons, D. A. 1994, AJ, 108, 1437
Henry, T. J., & McCarthy, D. W., Jr. 1990, ApJ, 350, 334
Henry, T. J., Subasavage, J. P., Brown, M. A., Beaulieu, T. D., Jao, W.-C., & Hambly, N. C. 2004, AJ, 128, 2460
Herbst, T. M., Thompson, D., Fockenbrock, R., Rix, H.-W., & Beckwith, S. V. W. 1999, ApJ, 526, L17
Hogg, D. W., Finkbeiner, D. P., Schlegel, D. J., & Gunn, J. E. 2001, AJ, 122, 2129
Ivezić, Ž., et al. 2004, Astron. Nachr., 325, 583
Ivezić, Ž., et al. 2007, AJ, 134, 973
Ivezić, Z., et al. 2008, ApJ, 684, 287
Joergens, V. 2006, A&A, 448, 655
Johnson, J. A., & Apps, K. 2009, ApJ, 699, 933
Jurić, M., et al. 2008, ApJ, 673, 864
Kerr, F. J., & Lynden-Bell, D. 1986, MNRAS, 221, 1023
King, I., Gilmore, G., & van der Kruit, P. C. (ed.) 1990, The Milky Way As Galaxy (Mill Valley, CA: Univ. Science Books)
Kirkpatrick, J. D., Henry, T. J., & Simons, D. A. 1995, AJ, 109, 797
Kirkpatrick, J. D., et al. 1999, ApJ, 519, 802
Kowalski, A. F., Hawley, S. L., Hilton, E. J., Becker, A. C., West, A. A., Bochanski, J. J., & Sesar, B. 2009, AJ, 138, 633
Kroupa, P. 2002, Science, 295, 82
Kroupa, P., Tout, C. A., & Gilmore, G. 1990, MNRAS, 244, 76
Kroupa, P., Tout, C. A., & Gilmore, G. 1993, MNRAS, 262, 545
Lada, C. J. 2006, ApJ, 640, L63
Larson, R. B. 1981, MNRAS, 194, 809
Larson, R. B. 2005, MNRAS, 359, 211
Laughlin, G., Bodenheimer, P., & Adams, F. C. 1997, ApJ, 482, 420
Lépine, S., Rich, R. M., & Shara, M. M. 2003, AJ, 125, 1598
Lépine, S., & Scholz, R.-D. 2008, ApJ, 681, L33
Luhman, K. L. 2004a, ApJ, 617, 1216
Luhman, K. L. 2004b, ApJ, 614, 398
Luhman, K. L. 2006, ApJ, 645, 676
Luhman, K. L., Mamajek, E. E., Allen, P. R., Muench, A. A., & Finkbeiner, D. P. 2009, ApJ, 691, 1265
Lupton, R., Gunn, J. E., Ivezić, Z., Knapp, G. R., & Kent, S. 2001, in ASP Conf. Ser. 238, Astronomical Data Analysis Software and Systems X, ed. F. R. Harnden, Jr., F. A. Primini, & H. E. Payne (San Francisco, CA: ASP), 269
Lutz, T. E., & Kelker, D. H. 1973, PASP, 85, 573
Luyten, W. J. 1939, Publications of the Astronomical Observatory, University of Minnesota, Vol. 2 (Minneapolis, MN: Univ. Minnesota Press), 121
Luyten, W. J. 1941, in New York Academy Sciences Annals, The Fundamental Properties of the Galactic System, Vol. 42, ed. E. M. Schlaikjer & J. Schilt (New York: The New York Academy of Sciences), 201
Luyten, W. J. 1968, MNRAS, 139, 221
Luyten, W. J. 1979, LHS Catalogue. A Catalogue of Stars with Proper Motions Exceeding 0″5 Annually (2nd ed.; Minneapolis, MN: Univ. Minnesota)
Majewski, S. R., Skrutskie, M. F., Weinberg, M. D., & Ostheimer, J. C. 2003, ApJ, 599, 1082
Malmquist, K. G. 1936, Stockholm Obs. Medd., 26
Marshall, D. J., Robin, A. C., Reylé, C., Schultheis, M., & Picaud, S. 2006, A&A, 453, 635
Martini, P., & Osmer, P. S. 1998, AJ, 116, 2513
McCuskey, S. W. 1966, Vistas Astron., 7, 141
Miller, G. E., & Scalo, J. M. 1979, ApJS, 41, 513
Monet, D. G., Dahn, C. C., Vrba, F. J., Harris, H. C., Pier, J. R., Luginbuhl, C. B., & Ables, H. D. 1992, AJ, 103, 638
Moraux, E., Bouvier, J., Stauffer, J. R., Barrado y Navascués, D., & Cuillandre, J. 2007, A&A, 471, 499
Moraux, E., Kroupa, P., & Bouvier, J. 2004, A&A, 426, 75
Ng, Y. K., Bertelli, G., Chiosi, C., & Bressan, A. 1997, A&A, 324, 65
Oliveira, J. M., Jeffries, R. D., & van Loon, J. T. 2009, MNRAS, 392, 1034
O'Mullane, W., Li, N., Nieto-Santisteban, M., Szalay, A., Thakar, A., & Gray, J. 2005, arXiv:cs/0502072
Padoan, P., Juvela, M., Goodman, A. A., & Nordlund, Å. 2001, ApJ, 553, 227
Padoan, P., Nordlund, A., & Jones, B. J. T. 1997, MNRAS, 288, 145
Padoan, P., & Nordlund, Å. 2002, ApJ, 576, 870
Pier, J. R., Munn, J. A., Hindsley, R. B., Hennessy, G. S., Kent, S. M., Lupton, R. H., & Ivezić, Ž. 2003, AJ, 125, 1559

Press, W. H., Teukolsky, S. A., Vetterling, W. T., & Flannery, B. P. 1992, Numerical Recipes in FORTRAN. The Art of Scientific Computing (2nd ed.; Cambridge: Cambridge Univ. Press)

Reid, I. N. 1997, AJ, 114, 161

Reid, I. N., & Cruz, K. L. 2002, AJ, 123, 2806

Reid, I. N., & Gizis, J. E. 1997, AJ, 113, 2246

Reid, I. N., Gizis, J. E., & Hawley, S. L. 2002, AJ, 124, 2721

Reid, I. N., & Hawley, S. L. (ed.) 2005, New Light on Dark Stars Red Dwarfs, Low-Mass Stars, Brown Stars (Berlin: Springer)

Reid, I. N., Hawley, S. L., & Gizis, J. E. 1995, AJ, 110, 1838

Reid, I. N., et al. 1999, ApJ, 521, 613

Reid, I. N., et al. 2003, AJ, 125, 354

Salpeter, E. E. 1955, ApJ, 121, 161

Sandage, A. R., & Eggen, O. J. 1959, MNRAS, 119, 278

Scalo, J. M. 1986, Fundam. Cosm. Phys., 11, 1

Schlegel, D. J., Finkbeiner, D. P., & Davis, M. 1998, ApJ, 500, 525

Schultheis, M., Robin, A. C., Reylé, C., McCracken, H. J., Bertin, E., Mellier, Y., & Le Fèvre, O. 2006, A&A, 447, 185

Scoville, N., et al. 2007, ApJS, 172, 1

Sesar, B., Ivezić, Ž., & Jurić, M. 2008, ApJ, 689, 1244

Shkolnik, E., Liu, M. C., & Reid, I. N. 2009, ApJ, 699, 649

Siegel, M. H., Majewski, S. R., Reid, I. N., & Thompson, I. B. 2002, ApJ, 578, 151

Skrutskie, M. F., et al. 2006, AJ, 131, 1163

Smith, J. A., et al. 2002, AJ, 123, 2121

Stobie, R. S., Ishida, K., & Peacock, J. A. 1989, MNRAS, 238, 709

Stoughton, C., et al. 2002, AJ, 123, 485

Strauss, M. A., et al. 1999, ApJ, 522, L61

Tinney, C. G. 1993, ApJ, 414, 279

Tucker, D. L., et al. 2006, Astron. Nachr., 327, 821

van Altena, W. F., Lee, J. T., & Hoffleit, E. D. 1995, The General Catalogue of Trigonometric [Stellar] Parallaxes (4th ed. (completely revised and enlarged); New Haven, CT: Yale University Observatory)

van Leeuwen, F. 2007, A&A, 474, 653

van Rhijn, P. J. 1925, Publications of the Kapteyn Astronomical Laboratory Groningen, Vol. 38 (Groningen, The Netherland: Hoitsema Brothers), D1

van Rhijn, P. J. 1936, Publications of the Kapteyn Astronomical Laboratory Groningen, Vol. 47 (Groningen, The Netherland: Hoitsema Brothers), 1

Vrba, F. J., et al. 2004, AJ, 127, 2948

West, A. A., Hawley, S. L., Bochanski, J. J., Covey, K. R., Reid, I. N., Dhital, S., Hilton, E. J., & Masuda, M. 2008, AJ, 135, 785

West, A. A., Walkowicz, L. M., & Hawley, S. L. 2005, PASP, 117, 706

West, A. A., et al. 2004, AJ, 128, 426

Wielen, R. 1974, Highlights of Astronomy, Vol. 3 (Dordrecht: Reidel) 395

Wielen, R., Jahreiss, H., & Krüger, R. 1983, in IAU Colloq. 76, Nearby Stars and the Stellar Luminosity Function, ed. A. G. D. Philip & A. R. Upgren (Schenectady, NY: L. Davis Press) 163

Williams, C. C., et al. 2002, BAAS, 34, 1292

Willman, B., et al. 2005, AJ, 129, 2692

Woolf, V. M., & Wallerstein, G. 2006, PASP, 118, 218

Yanny, B., et al. 2003, ApJ, 588, 824

York, D. G., et al. 2000, AJ, 120, 1579

Zheng, Z., Flynn, C., Gould, A., Bahcall, J. N., & Salim, S. 2001, ApJ, 555, 393

ERRATUM: "THE LUMINOSITY AND MASS FUNCTIONS OF LOW-MASS STARS IN THE GALACTIC DISK. II. THE FIELD" (2010, AJ, 139, 2679)

John J. Bochanski[1,2], Suzanne L. Hawley[1], Kevin R. Covey[3], Andrew A. West[2,4], I. Neill Reid[5],
David A. Golimowski[5], and Željko Ivezić[1]
[1] Astronomy Department, University of Washington, P. O. Box 351580, Seattle, WA 98195, USA; jjb@mit.edu
[2] Kavli Institute for Astrophysics and Space Research, Massachusetts Institute of Technology, Building 37, 77 Massachusetts Avenue, Cambridge, MA 02139, USA
[3] Department of Astronomy, Cornell University, Ithaca, NY 14853, USA
[4] Department of Astronomy, Boston University, 725 Commonwealth Avenue, Boston, MA 02215, USA
[5] Space Telescope Science Institute, 3700 San Martin Drive, Baltimore, MD 21218, USA
Received 2012 March 28; published 2012 May 15

We report a sign error in the M_r, $r - i$ color–magnitude relation in Table 4 of the published paper. The correct relation is given in Table 1 below. The results in the published paper are unchanged as the error appeared only in the transcription of the relation in the original table. We regret any confusion this may have caused and thank Andrew Becker and Beth Willman for pointing out the discrepancy.

Table 1
Color–Absolute Magnitude Relations in the *ugriz* System

Absolute Magnitude	Color Range	Best Fit	σ_{M_r}
M_r	$0.50 < r - z < 4.53$	$5.190 + 2.474\,(r - z) + 0.4340\,(r - z)^2 - 0.08635\,(r - z)^3$	0.394
M_r	$0.62 < r - i < 2.82$	$5.025 + 4.548\,(r - i) + 0.4175\,(r - i)^2 - 0.18315\,(r - i)^3$	0.403
M_r	$0.32 < i - z < 1.85$	$4.748 + 8.275\,(i - z) + 2.2789\,(i - z)^2 - 1.5337\,(i - z)^3$	0.481